

Raman spectroscopic measurements and imaging on sub-newton Berkovich and spherical imprints in fused silica

Y.B. Gerbig, Chris A. Michaels

National Institute of Standards and Technology (NIST), Material Measurement Laboratory, 100 Bureau Drive, Gaithersburg, MD 20899, United States

Yvonne Gerbig <https://orcid.org/0000-0002-8947-4215>

Chris Michaels <https://orcid.org/0000-0002-6562-4848>

Corresponding author: yvonne.gerbig@nist.gov

Abstract

This paper lays out best practices for evaluating and optimizing a Raman spectroscopy setup to ensure the collection of reliable spectral data and/or Raman images on indented glasses. The Raman spectroscopic measurements and imaging were conducted on residual imprints created with Berkovich and spherical probes at forces in the sub-newton range in fused silica. The capability of a conventional optical instrument for mapping spectral variations in sub-newton imprints on glasses is evaluated by studying the influence of the optical configuration (choice of microscope objective) on the spatial resolution of the spectroscopy setup. The spatial resolution was quantitatively assessed in *Z* profile measurements and qualitatively evaluated by mapping changes in spectral features and correlated densification within the indented regions of fused silica specimens. The paper discusses the importance of appropriately matching the analysis volume of the Raman spectroscopic setup with the size of the indentation-induced densification zone by demonstrating the detrimental effects a mismatch may have on accurately capturing the magnitude of spectral changes and correlated densification.

Keywords: Fused silica, Indentation, Densification, Raman imaging, Raman spectroscopy

1 Introduction

Amorphous materials with an open network structure exhibit an anomalous plastic response to mechanical loading, that is characterized by the complex interactions of deformation mechanisms such as volume-changing densification and volume-conservative plastic shear flow.[1-3] As such, it is challenging to establish relationships between atomic scale processes and continuum scale descriptions of the mechanical

behavior (constitutive laws) for such glasses.[2,4] Over the decades, various constitutive models have been developed to describe the plasticity of fused silica under different types of mechanical loading, such as pure hydrostatic compression,[5,6] pure shear,[5,7] or mixed pressure-shear loading.[2,3,8-11]

Indentation testing may help in the validation and (if necessary) revision of proposed constitutive laws for modeling the plastic deformation of glasses, as hydrostatic pressures combined with shear stresses are generated during indentation experiments. [3,12-15] However, indentation (force-displacement) curves by themselves do not validate a constitutive law and must be complemented by richer data sets (e.g., measurements of strain distributions or densification gradients) to advance the constitutive modelling of glass plasticity.[3,10,12,15] Raman spectroscopic imaging/scanning has been employed in recent years to map changes in spectral parameters in and around residual imprints and to correlate the spectral changes to variations in the structural compaction (densification) of the indented glass.[12,16-20] Most of the Raman mapping experiments were conducted on residual micro-indentations created by forces ranging from a few to several tens of Newtons due to limitations in the spatial resolution of the Raman spectroscopy configurations used in these studies.[12,17]

One issue of mapping large-sized high-load indentations is the constraint on the resolution (data point density) of the collected Raman images. With glasses being commonly weak Raman scatterers, long times are required to collect individual Raman spectra (individual data points in image) of satisfactory quality. Collection times from 1 min up to 25 min per spectrum have been reported for previous Raman imaging studies of indented glasses.[12,17,18] This limits the total number of spectra (data points) measurable before mechanical/thermal drift affects the image collection. As consequence, only sections instead of entire residual imprints were usually mapped.[12,16,18]

However, the major drawback of mapping high-load indentations, especially when conducted with the acute Berkovich or Vickers probes typically used in glass indentations, is the frequent occurrence of severe cracking in close proximity to the imprints.[21] Different fracture patterns have been observed on indented glasses: cone cracks, radial-median cracks, lateral cracks and edge cracks.[22-24] Edge cracks are characterized by cracks parallel to and very near the contact periphery that extend vertically to shallow depths (small fraction of the depth of residual imprint).[24] Since this type of cracks are confined to the very-near surface region, they will probably not interfere with Raman measurements (determination of spectral shifts).[11] In contrast, the other mentioned crack systems can affect the spectroscopic measurements significantly, as they are much more pronounced and penetrate the glass specimen to depths several times larger than the depth of the residual imprint.[24-28] As such, these crack systems can introduce local shape modifications and thereby affect the expected laser spot position in Raman measurements.[11] Additionally, cracking may increase the scattering of the laser beam and thereby degrade the spectroscopic measurement due to undesirable expansion of the analysis volume. Furthermore,

the elastic-strain release upon crack formation may hamper how accurately the actual degree of densification can be captured.[17] All of which can impede the spectroscopic characterization of the true shape, size, and nature of the densification zone of the indented glasses.

For fused silica (FS), the glass type studied in this paper, the force threshold for radial cracking was determined to be well above 500 mN for Berkovich and Vickers indentations.[21,24,29-31] This also means that the formation of lateral and median cracks is precluded below this threshold, as sub-surface cracking is only observed in combination with radial cracking.[24] The force threshold for inducing cone cracks in FS was determined to be 250 mN in a recent study of Vickers indentations.[32] Though indentation forces larger than 1700 mN are required to observe this crack pattern with regularity (probability of occurrence > 50 %); the probability to initiate cone cracks at 500 mN has been reported to be only 15% (Fig. 2 in [32]). Consequently, to avoid measurement-interfering cracking, the indentation forces should be limited to the sub-Newton range (preferably below 500 mN) to create residual imprints in fused silica for spectroscopic analysis. Then again, the imprints created at milli-newton forces are commonly believed to be too small in size to allow mapping of variations in densification in the indented glass region due to the insufficient spatial resolution of conventional Raman spectroscopy configurations.[11,12,14,15,17] If the spatial resolution is too coarse, the spectral information from regions in different states of densification get convoluted leading to a misrepresentation of the indentation-induced spectral and associated structural changes.[11,13,33]

The lateral and depth spatial resolution inherent to a Raman spectroscopic measurement are determined by the optical configuration and components used in the Raman setup. Among other factors, the quality of the spectral data collected depends on the microscope objective used to focus the laser beam on the specimen and to collect the Raman scattering. In particular, under appropriate confocal conditions, the numerical aperture (NA) of the objective together with the wavelength of the laser beam (λ) determine the waist (or lateral spot diameter LD) and depth for the focus (DOF). For an idealized diffraction limit, LD is $\approx 1.22 \cdot \lambda/NA$. [34] The theoretical DOF is $\approx 4 \cdot n \cdot \lambda/NA^2$, where n is the refractive index of the material.[34] It should be mentioned that various methods to experimentally determine the spatial resolution of a Raman spectroscopy setup have been proposed in the past.[35] This methods require the preparation of specific test structures replicating the optical properties (refractive index) of the materials to be spectroscopically analyzed. The spectral resolution can be optimized by adapting the optical configuration of the Raman microscope and, thus, enable a reliable (*in-situ*) spectroscopic characterization of the densified regions of milli-newton indentations, as has been recently demonstrated for a custom-built setup.[33,36]

In this paper, the capability of a conventional optical instrument for mapping spectral variations (changes in densification) in sub-newton imprints is assessed by studying the influence of the optical configuration (choice of microscope objective) on the spatial resolution of the spectroscopy setup.

The spatial resolution (in terms of analysis area) is quantitatively assessed in Z profile measurements and qualitatively evaluated by mapping changes in the spectral features and correlated densification within the indented regions of fused silica. Fused silica was selected as test material in this study because it embodies the model material for disordered networks and often serves as a reference material in glass studies, in addition to being a technologically important material.[2,24,32,37] The Raman spectroscopic measurements and imaging were conducted on residual imprints created at forces in the sub-newton range in indentations with Berkovich and spherical probes. Compared to the Berkovich (and Vickers) probes, spherical indentation allows for study of the deformation behavior as a function of the indentation strain due to the non-self-similar geometry of spherical probes.[33,38] Furthermore, simpler analytical models can be employed for interpretation and simulation due to the axisymmetry of the strain fields generated by spherical probes.[38] This is, to our knowledge, the first time Raman images of spherical glass imprints have been collected.

This paper will further discuss the importance of appropriately matching the analysis area of the Raman spectroscopy setup with the size of the indentation-induced densification zone by demonstrating the detrimental effects a mismatch may have on accurately capturing the magnitude and distribution of spectral changes. For the purpose of this study, the term densification zone describes the region of the indented glass where indentation-induced stresses and strains caused structural changes to the glass network commonly referred to a compaction or densification (level of densification may vary within the densification zone). The dimension of the densification zone and the maximum level of densification within this zone are the main focus of this paper. Finally, the paper will lay out best practices for evaluating and optimizing a Raman spectroscopy setup by (quantitatively) assessing its spatial resolution to ensure the collection of meaningful spectral data/images on indented glasses.

2 Experimental procedures

2.1 Preparation of residual indents for Raman spectroscopic analysis

The glass sample indented and spectroscopically analyzed in this study was made of optically polished, Corning 7980 UV Grade fused silica (FS) (Valley Design Corporation, Shirley, MA). The FS sample had a cylindrical shape with a diameter of 25.4 mm and a thickness of 1 mm.

To generate residual imprints for the Raman measurements/imaging, the FS sample was indented using two probes of different acuity and shape: a diamond Berkovich probe and a conospherical diamond probe with a nominal tip curvature of 5 μm . The tip-area functions of these probes and the machine compliance for an individual sample-probe combination were determined in separate indentation experiments according to common procedures.[39,40]

TAB. 1: Maximum indentation depth (h_{\max}), residual depth (h_r), radius of spherical imprint (a), length of side of Berkovich imprint (s) and estimated thickness of the densification zone ($z_{d,s}$) for contact impressions generated at various indentation forces F with Berkovich and spherical probes. The maximum values for the D_2 shift and the $\Delta\sigma$ shift are shown as determined in the Z profile and mapping experiments at various loads. Spectral data based on measurements with the NA 0.5 objective (where applicable) are marked with “*”. The values σ_0 and $\omega_{D_2,0}$ mark the σ parameter and wavenumber of the D_2 band of the unperturbed bulk, respectively. The spectral shift error estimates are based on the standard deviation of repeat spectral measurements of the relevant specimen coupled with an assessment of focal position errors. For the other data, the values given represent the average \pm standard deviation in measurements on three indentations. Equations (1) to (5) are shown in section 4.1.

Indentations with Berkovich probe					
F (mN)		10	50	100	300
h_{\max} (nm)		303 ± 9	677 ± 5	953 ± 6	1647 ± 3
h_r (nm)		174 ± 10	345 ± 10	476 ± 6	823 ± 2
s (μm)		1.66 ± 0.12	3.87 ± 0.04	5.29 ± 0.03	9.23 ± 0.02
$z_{d,s}$ (μm)	eqn. (1)	0.9 ± 0.01	1.9 ± 0.01	2.6 ± 0.00	4.6 ± 0.00
	eqn. (2)	0.8 ± 0.03	1.6 ± 0.02	2.3 ± 0.01	3.9 ± 0.01
	eqn. (3)	0.7 ± 0.04	1.3 ± 0.01	1.8 ± 0.01	3.1 ± 0.01
	eqn. (4)	0.5 ± 0.03	1.0 ± 0.03	1.3 ± 0.00	2.3 ± 0.00
Max. $\Delta\sigma$ (cm^{-1})	profile	25 ± 1	36 ± 1	49 ± 2	76 ± 2
	map	-	-	-	$77 \pm 2; 7 \pm 2^*$
Max. D_2 shift (cm^{-1})	profile	10 ± 1	12 ± 1	14 ± 1	17 ± 1
	map	-	-	-	$18 \pm 1; 3 \pm 1^*$
σ_0 : $407 \pm 1 \text{ cm}^{-1}; 407 \pm 1 \text{ cm}^{-1*}$					
$\omega_{D_2,0}$: $602 \pm 1 \text{ cm}^{-1}; 601 \pm 1 \text{ cm}^{-1*}$					
Indentations with spherical probe					
F (mN)		50	100	150	200
h_{\max} (nm)		456 ± 3	719 ± 4	956 ± 7	1139 ± 8
h_r (nm)		41 ± 1	182 ± 4	324 ± 12	386 ± 15
a (μm)		1.31 ± 0.01	1.84 ± 0.01	2.34 ± 0.02	2.64 ± 0.02
$z_{d,s}$ (μm)	eqn. (5)	0.2 ± 0.01	1.0 ± 0.02	1.8 ± 0.07	2.1 ± 0.08
Max. $\Delta\sigma$ (cm^{-1})	profile	5 ± 1	30 ± 1	44 ± 1	$51 \pm 2; 4 \pm 2^*$
	map	-	-	-	$52 \pm 2; 5 \pm 2^*$
Max. D_2 shift (cm^{-1})	profile	2 ± 1	9 ± 1	12 ± 1	$13 \pm 1; 2 \pm 1^*$
	map	-	-	-	$13 \pm 1; 2 \pm 1^*$
σ_0 : $411 \pm 1 \text{ cm}^{-1}; 407 \pm 1 \text{ cm}^{-1*}$					
$\omega_{D_2,0}$: $602 \pm 1 \text{ cm}^{-1}; 601 \pm 1 \text{ cm}^{-1*}$					

To stay below the thresholds for crack initiation, residual imprints were generated in indentations at 10 mN, 50 mN, 100 mN and 300 mN with the Berkovich probe and at 50 mN, 100 mN, 150 mN and 200 mN with the conospherical probe, using an instrumented indentation instrument (Hysitron TriboIndenter®, Bruker, Minneapolis, MN). The loading and unloading rates were set to be 10 mN/s for all indentations. Three indentations were made per indentation force with the imprints arranged along a straight line and spaced 50 μm apart. The lines of imprints generated at different loads were also spaced at least 50 μm apart.

The indentation curves generated in this study were corrected for machine compliance following procedures for Berkovich and spherical probes described elsewhere.[40,41] From the compliance-corrected curves, values for the maximum indentation depth (h_{max}) and residual depth (h_r) were obtained for each indentation. As relevant dimensional features of the residual imprints, the contact radius (a) of spherical imprints and the side length of Berkovich imprint (s) were determined via the approach proposed by Field and Swain[42] or (via the contact area calculated) with the Oliver-Pharr method,[43] respectively. The calculated values of a and s were verified by measurements on optical micrographs of the residual imprints. The individual compliance-corrected indentation curves and optical micrographs of the residuals were summarized in the data publication [44] associated with this study.

The average and standard deviation of the indentation-related parameters were determined from the three indentations conducted at the same indentation force and were summarized in Tab. 1 for the two probe geometries.

2.2 Raman spectroscopic measurements on residual indents

Configuration of Raman microscope

The custom Raman microscope used in this study is quite similar to those reported in earlier work on narrow band luminescence microscopy[45] and confocal Raman microscopy[46] thus only noteworthy modifications to those designs are discussed. The excitation source utilized is a single longitudinal mode, diode pumped, solid state 532 nm laser (Coherent Verdi). The light is delivered into the microscope enclosure with a single mode fiber and filtered through a laser-line transmission filter (Semrock). The light is then reflected from a long pass Raman filter (Semrock) in an inject-reject geometry onto the back aperture of the microscope objective. A beam expander is used in the excitation beam path to ensure that the back apertures of the objectives are filled. As has been discussed in a previous *in-situ* Raman spectroscopic study of FS,[33,36] the relatively low intensity of Raman scattering in FS requires the use of significant laser powers, on the order of 100 mW through the microscope objective.

Two metallurgical objectives are used in this work: an MPlanApo, 0.95 NA objective (Olympus) and an LMPlanFL N 0.5 NA objective (Olympus). As mentioned in the introduction, the NA of the objective determines the LD and the DOF of the collection volume, hence, the volume of the sample analyzed in

Raman spectroscopy measurement. For $\lambda = 532$ nm, the LD is $0.68 \mu\text{m}$ and $1.30 \mu\text{m}$ for the NA 0.95 and NA 0.5 objectives, respectively. The DOF is $2.36 \mu\text{m}$ and $8.51 \mu\text{m}$ for the NA 0.95 and NA 0.5 objectives in air ($n = 1$), respectively. It should be noted that these values have been calculated for ideal conditions. The actual values are undoubtedly larger and may vary within the indent due to scattering and refraction phenomena. In particular, the DOF might be considerably extended and variable when focusing through the glass specimen in the Z profile experiments as the refractive index of FS is significantly larger than that of air and density dependent:[84] $n = 1.46$ for 2.2 g/cm^3 (pristine), $n = 1.55$ for 2.66 g/cm^3 ($\approx 21\%$ densified). The Raman scattered photons are collected in an epi configuration and are passed through a second long pass Raman filter (Semrock) prior to being coupled into a transport fiber. A single mode optical fiber with a mode field diameter of $4.1 \mu\text{m}$ (SM450, Thorlabs) was used in conjunction with the NA 0.95 objective while a multimode optical fiber with a mode field diameter of $50 \mu\text{m}$ (M42L02, Thorlabs) was used with the NA 0.5 objective. In each case, the fiber core acted as a confocal aperture and the fiber was used to transport the detected photons to a 0.5 m imaging spectrograph equipped with a 1200 g/mm grating blazed at 500 nm (Acton SP2-500i) and a liquid nitrogen cooled CCD camera (Princeton Instruments). In the previous *in-situ* Raman study on FS, subtle day to day variations in the instrumental sensitivity in the low wavenumber region of the spectra due to polarization effects of the transport fiber were observed. As in that work, an achromatic depolarizer (DPU-25, Thorlabs) was placed in the entrance optics of the spectrograph to avoid this effect. All of the spectra in this paper were corrected for the spectral intensity instrument response function with Standard Reference Material 2242 and the published procedure (2242 Certificate). The absolute wavelength of the laser was measured daily with a wavemeter (Coherent) to allow the spectral calibration of the CCD camera using the atomic emission line positions for a Ne discharge lamp.[47]

Procedure for collecting Z profiles

In the Z profile experiments, the distance of the microscope objective from the indented specimen is initially adjusted so that the laser beam is focused on the specimen surface just outside the indent area. This distance is then denoted as z axis focal position zero. A sequence of spectra is then acquired with the laser centered on the residual imprint. The first spectrum in the sequence is acquired with the focal position equal to positive $1 \mu\text{m}$ (beam focus $1 \mu\text{m}$ above the specimen surface). Eleven more spectra are collected with the focal position descending into the specimen in $1 \mu\text{m}$ increments (i.e., the second spectrum is at focal position zero, the third at $-1 \mu\text{m}$ and so on until the last spectrum at $-10 \mu\text{m}$). These Z profile sequences were collected with the NA 0.95 objective for each indentation load, for both the Berkovich and spherical imprints, with an acquisition time of 180 s. A single Z profile sequence was collected with the NA 0.5 objective for the 200 mN spherical imprint using a 10 s acquisition time. It is worth noting that the actual

focus might be somewhat displaced from the z position expected due to the use of a metallurgical objective focusing into glass and possible effects of the imprint geometry on the focal position and shape.

Note that the positive 1 μm focal position spectrum is used simply to check that the peak spectral intensity is measured with the focal position at the specimen surface, as would be expected for a well-aligned microscope. The expected peak spectral intensity with focal position was observed in all sequences recorded with the NA 0.95 objective.

Procedure for ex-situ Raman mapping

Raman maps of each imprint were acquired by scanning the sample over a square area of a size chosen to adequately encompass the indented area. The sample z axis position was set such that the excitation beam was focused on the sample surface just outside the indented area. The z axis position was held constant for the entirety of the scan. A dynamic adjustment of the focus that follows the contour of the residual impression during the scan was outside the scope of the paper and not implemented in the Raman setup. This might affect the spectral data collected in deeper regions of the impression ($> 1 \mu\text{m}$ in this study). Despite the long map acquisition times (up to ~ 12 hours) the amount of observed beam focus drift did not meaningfully impact the measurements, due to the excellent mechanical stability of the microscope. The Raman spectra were acquired on an evenly spaced grid across the scan area. These scan areas ranged from 4 μm to 12 μm depending on the size of the imprint. In order to minimize the total map acquisition time while still achieving a desirable level of spatial sampling, the number of spectra acquired across each grid row was chosen as either 24 points or 32 points. The acquisition times per spectra were chosen to achieve adequate signal to noise while again minimizing the overall map acquisition time. Maps acquired with the NA 0.95 objective required 40 s per spectrum while the NA 0.5 objective maps only required 10 s spectral acquisition times. Maps were acquired for each load for both the spherical and Berkovich imprints with the NA 0.95 objective as well as for a smaller subset of imprints with the 0.5 NA objective. Duplicate maps of selected imprints were also acquired to assess measurement reproducibility.

All raw spectral data collected in the Z profile and Raman mapping experiments have been compiled in a separate data publication.[44]

2.3 Analysis of Raman spectroscopic data

Indentation induced spectral changes and their correlation to densification

The Raman spectra collected in pristine regions of the glass sample (see also bulk spectra in Fig. 1b, c) showed the characteristic spectral features of FS reported in literature [48-58]:

- a broad, asymmetric main band (MB), frequently referred to as the R band, located at 430 cm^{-1} ,
- two narrow Raman peaks located around 495 cm^{-1} and 606 cm^{-1} , often labelled in the literature as defect bands D_1 and D_2 , respectively,

- an asymmetric band (A band) located at 800 cm^{-1} , and
- a doublet (DB) of bands located at 1060 cm^{-1} and 1200 cm^{-1} .

Being an anomalous glass, FS deforms primarily by densification and to a lesser degree by shear during indentation (below the fracture threshold).[59] The mechanisms which with indentation-induced densification and shear affect the different structure length scales of the silicate network are still under investigation.[20,60-62] However, indentation-induced changes to the glass structure distinctly alter the spectral profile of indented FS.[11,12,19,20,33] Compared to its pristine state, the following spectral changes were observed in the indented region of FS imprints: The position of the MB shifted to higher wavenumbers and merged with the D_1 band. Also, the position of the D_2 band shifted slightly to higher wavenumbers and its intensity increased relative to MB. The shape of the A band became more symmetrical with its width broadening. The DB bands shifted to smaller wavenumbers.

Several studies have linked variations in spectral regions with changes in density or the densification ratio of FS. For example, Perriot *et al.*[12] proposed an empirical relationship between the densification ratio ($=$ density of sample in densified state / initial density of sample in unperturbed state) and the wavenumber ratio of the D_2 band ($= \omega_{D_2}$ of densified sample / ω_{D_2} of unperturbed glass). Deschamps *et al.* found the shift of the parameter σ to be proportional to degree of densification under hydrostatic compression at room temperature.[37] The parameter σ is defined as the wavenumber at which the integral over the background corrected spectral region (200 cm^{-1} to 700 cm^{-1}) encompassing the MB, D_1 and D_2 bands reaches half of its total value. It was suggested that the proposed correlation between σ and the densification ratio to be equally applicable to indentations.

The structure of densified glass is dependent on the process under which the densification occurred.[65-67] For a potentially process-independent calibration, Cornet *et al.* suggested correlating the densification with the low-wavenumber half width at half maximum $L_{1/2}$ of the main band.[68]

Determination of spectral parameters and densification

As the most commonly analyzed spectral parameters, the relative σ and the D_2 shift, are the focus of analysis in this study. However, data for the MB position and $L_{1/2}$ were also compiled and can be found in the paper-accompanying data publication.[44]

Spectral parameters can be extracted from glass spectra recorded in either a Z profile sequence or from an individual spatial location in an image. The raw spectral data (camera pixel, counts) are converted to spectral points (wavenumber, Raman intensity) through application of the spectral calibration and the instrument response function correction procedures described in section 2.2.

The spectra are fit using non-linear least squares over the wavenumber range from $(182\text{ to }680)\text{ cm}^{-1}$ using a 6-band spectral model described by Chligui *et al.* [69] and utilized in our earlier publication on *in-situ*

Raman measurements of FS indentations.[33,36] While other spectral models might also be suitable, this model does an excellent job of representing the experimental spectra. The D_2 band is spectrally distinct from the main band that consists of several overlapping spectral features. Consequently, the position of the D_2 band center falls directly out of the best fit model and can be used to estimate the degree of densification via the relationship proposed by Perriot *et al.* [12]. For comparison purposes, the procedure described in [37] was also used in this study for obtaining the σ parameter. Thereby, σ is calculated by determining the total trapezoidal rule integral of the baseline corrected spectrum over the region from 182 cm^{-1} to 680 cm^{-1} , where a linear baseline is determined from the region endpoints. The wavenumber at which the integral reaches half of the total value is then designated σ . The two other spectral parameters that have been related to densification, the MB position and $L_{1/2}$, can also be readily extracted from the best fit spectral model. The MB position is extracted by finding the peak in the best-fit spectral model in the main band region by finding the zero-crossing point of the first derivative of the spectral intensity with respect to wavenumber. (Note that this procedure is not useful on the experimental spectral data due to intensity noise, so the best-fit function is utilized instead.) $L_{1/2}$ is calculated after determination of the main band position. It is defined as the half width at half maximum of the main band calculated on the low wavenumber side. This is done by finding the zero crossing of a function defined as the best fit spectral function minus half the intensity of the main band at its peak.

The observed spectral changes were correlated to the densification of the glass network using empirical equations based on previously published data [37,67,70,71] as described in the Supplemental Material (see section S1, Tab. S2, Fig. S1). The density changes presented in this paper were based on the relative σ and the D_2 shifts. It should be noted that the densification in the indented region is discussed in this paper in relative rather than absolute terms, e.g., the density changed by + 10 % from the initial state of the analyzed specimen rather than the specimen was 10 % densified. To calculate an absolute densification ratio based on changes to a particular spectral parameter, the reference value characterizing the non-densified state of FS has to be known for that parameter. However, such reference values have yet to be established and spectral parameters measured for a non-densified FS specimen cannot be universally applied across laboratories due to experimental and instrument differences.[72]

3 Results

In the following sections, the results of the Z profile and mapping experiments are summarized.

3.1 Z profile experiments

Z profile measurements on high-load spherical imprints

The densified material with its altered spectral profile (see section 2.3) is concentrated in a finite volume beneath the surface of the contact impression. Using this fact, Z profile measurements were conducted to

assess the capability of an optical setup to detect the densification-related spectral changes in glass imprints.[11,33,36] It should be noted that the purpose of these measurements is simply to determine the expansion of the densification zone along the z-axis and not to determine a density gradient within the densification zone.

In Z profile experiments, a series of Raman measurements were conducted in the center of the imprint with the focal plane of the microscope objective being shifted stepwise along the z axis, starting 1 μm above the surface of the samples and ending 10 μm into the specimen bulk. Note that in all confocal measurements there is an out-of-focus contribution to the measured signal. Indeed, the purpose of using a confocal aperture is to reduce the relative contribution of this out-of-focus signal. In our Z profile scheme, the measured signal at $z = 1 \mu\text{m}$ has a large out-of-focus contribution relative to those at other z positions because the signal originates from an analysis volume above the sample (air) yielding little in-focus glass Raman signal. The signal intensity at $z = 1 \mu\text{m}$ is thus smaller than those for spectra taken at z positions at the surface and within the specimen ($z = 0$ through 10 μm) and dominated by the out-of-focus signal originating from beyond the densified region. This leads to the non-intuitive result that the spectra taken from above the specimen has a relatively large contribution from non-densified glass.

As densification-related changes in the FS are most prominently reflected in the main band region of the spectral profile, the σ parameter was extracted from each spectrum collected within the series. The value of σ_0 (measured in the unperturbed bulk region, Tab. 1) was then subtracted from the extracted σ values to determine the relative shift $\Delta\sigma$. A value of $\Delta\sigma = 0$ would indicate a non-densified state of the glass structure. The Z profile was generated by plotting the $\Delta\sigma$ values as function of the z-axis position at which individual spectra were collected.

Figure 1a shows the Z profiles collected with the NA 0.95 and NA 0.5 objectives at a residual imprint generated at 200 mN with the conospherical probe on the FS specimen. In addition, the dimension of the cross-section of the residual imprint are depicted with its depth scaled to the z axis. Also, the Raman spectrum collected at the specimen surface ($z = 0 \mu\text{m}$) on this high-load residual imprint was compared to the spectral profile of unperturbed FS (bulk specimen) for the NA 0.95 and NA 0.5 objectives in Figures 1b and 1c, respectively. The profiles shown were not baseline corrected.

The Z profiles for the two objectives differ significantly in their appearance. The shape of Z profile of the NA 0.95 objectives can be described as peaked: The relative shift initially increased, reached a maximum and then decreased with increasing z. The maximum relative shift of $\Delta\sigma_{\text{max}} = 51 \text{ cm}^{-1}$ was measured at the sample surface (at $z = 0 \mu\text{m}$). From this position onwards, the relative shift declines towards $\Delta\sigma = 0 \text{ cm}^{-1}$ and did not deviate from that value for focal positions beyond $z = -2 \mu\text{m}$. Such a trend was not observed for the Z profile of the NA 0.5 objective, which resembled a more gradual linear decline: The relative shift $\Delta\sigma$ decreased from its maximum of 4 cm^{-1} measured at $z = +1 \mu\text{m}$ to 0 cm^{-1} for $z < -6 \mu\text{m}$.

The maximum relative shift determined with the NA 0.5 objective was significantly smaller than for the NA 0.95 objective although the Raman measurements with both objectives were conducted in the same region of the residual imprint. The discrepancy in the $\Delta\sigma_{\max}$ values can be traced back to deviations between the spectral profiles collected with the two objectives: Compared to the bulk spectrum, the densification-related changes in position, shape and intensity of spectral bands were more pronounced in the Raman measurements with the NA 0.95 objective than with the NA 0.5 objective (see Figs. 1b and 1c). The Raman profile collected with NA 0.95 depicts the characteristic indentation-induced multiband alterations discussed earlier in the paper (see section 2.3). However, the Raman profile collected with NA 0.5 exhibits only marginal changes to width and height of the MB; the other glass bands appeared unaffected.

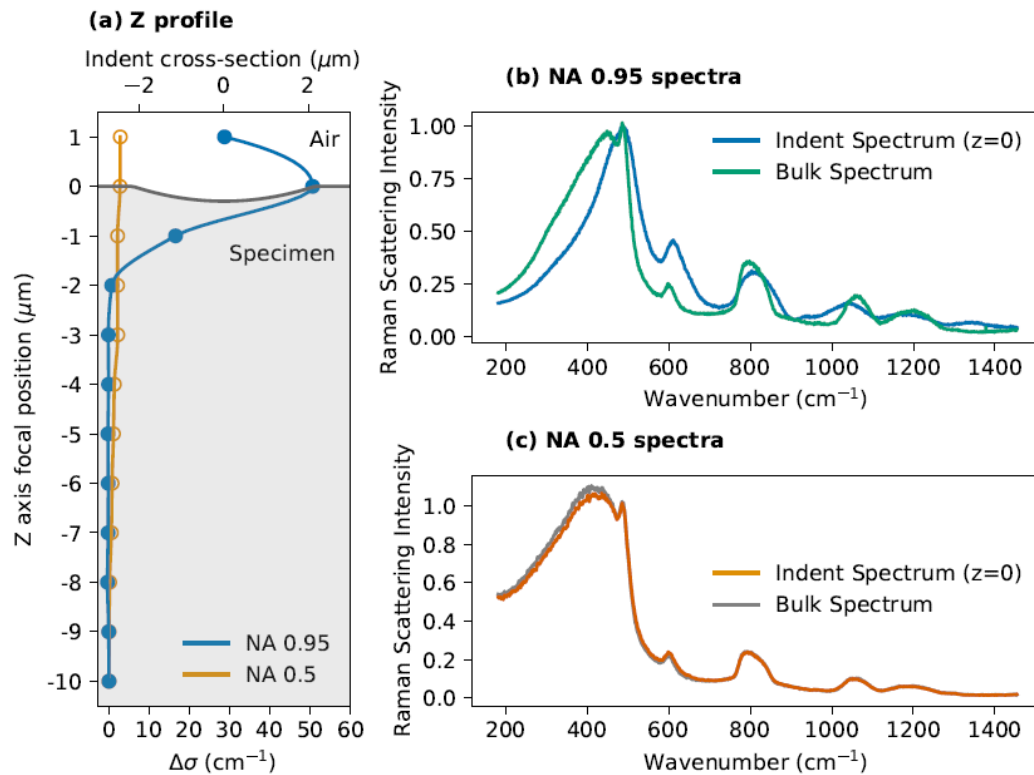


FIG. 1: (a) Z profiles collected with the NA 0.95 and NA 0.5 objectives at high-load spherical imprints that were generated at 200 mN with the conospherical probe on the FS specimen. The Z profiles were determined from Raman spectra collected in the center of the imprint with the focal plane being shifted stepwise along the z axis starting 1 μm above the surface ($z = 1 \mu\text{m}$) and ending 10 μm into the bulk of the specimen bulk ($z = -10 \mu\text{m}$). The figures also show a scaled sketch of the residual imprint (solid grey line). (b) Raman spectra collected with NA 0.95 objective at the specimen bulk and at center of residual of a 200 mN conospherical indentation at the focal position $z = 0 \mu\text{m}$. (c) Raman spectra collected with NA 0.95 objective at the specimen bulk and at center of the same residual at the focal position $z = 0 \mu\text{m}$. At diffraction

limit and for $n = 1$: NA 0.95: LD = 0.68 μm , DOF = 1.30 μm ; NA 0.5 objectives: DOF = 2.36 μm , DOF = 8.51 μm .

When further comparing the Z profiles of the two objectives, spectral deviations from the unperturbed bulk state ($\Delta\sigma \neq 0 \text{ cm}^{-1}$) were perceived at focal positions farther away from the residual imprint with the NA 0.5 objective than for the NA 0.95 objective and at depths that significantly exceeded the depth of the residual imprint (see Fig. 1a). This indicates that Raman measurements with the NA 0.5 objective characterized the spectral profile of the indented specimen region less accurately than the NA 0.95 objective. By underrepresenting the degree of and overstating the dimensional extent of indentation-induced spectral changes, any conclusions drawn from the spectral measurements with the NA 0.5 objective regarding the underlying structural change to the glass network may be highly misleading. Consequently, only the NA 0.95 objective was employed in additional Z profile measurements.

Z profile measurements on Berkovich and spherical imprints generated at different loads

Figure 2 shows the Z profiles collected with the NA 0.95 objective on residual imprints that were generated at different indentation loads with the Berkovich (Fig. 2a) and the spherical probes (Fig. 2b).

The position of the specimen surface in relation to the Z profile is indicated as a dotted line. For reference, the relative shift of the non-densified bulk ($\Delta\sigma = 0 \text{ cm}^{-1}$) is displayed as a thin grey line. All Z profiles collected with the NA 0.95 objective have a similar peaked appearance with $\Delta\sigma_{\text{max}}$ being located at a focal position of $z = 0 \text{ }\mu\text{m}$ (specimen surface). However, the magnitude of $\Delta\sigma_{\text{max}}$ appeared to increase with the indentation force at which the imprint was generated. At the residual Berkovich imprints, the following $\Delta\sigma_{\text{max}}$ values were determined in the Z profile measurements: 25 cm^{-1} (10 mN), 36 cm^{-1} (50 mN), 47 cm^{-1} (100 mN) and 76 cm^{-1} (300 mN). At the spherical imprints, the following $\Delta\sigma_{\text{max}}$ values were measured: 5 cm^{-1} (50 mN), 30 cm^{-1} (100 mN), 44 cm^{-1} (150 mN) and 51 cm^{-1} (200 mN). When shifting the focal position into the specimen bulk, the measured relative shift decreased and reached the non-densified bulk value at a focal position of $z = -2 \text{ }\mu\text{m}$ for most of the indentation forces, the exception being the smallest indentation forces (10 mN for the Berkovich imprints and 50 mN for the spherical imprints). In those cases, the bulk value was approached closer to the surface at focal position of $z = -1 \text{ }\mu\text{m}$.

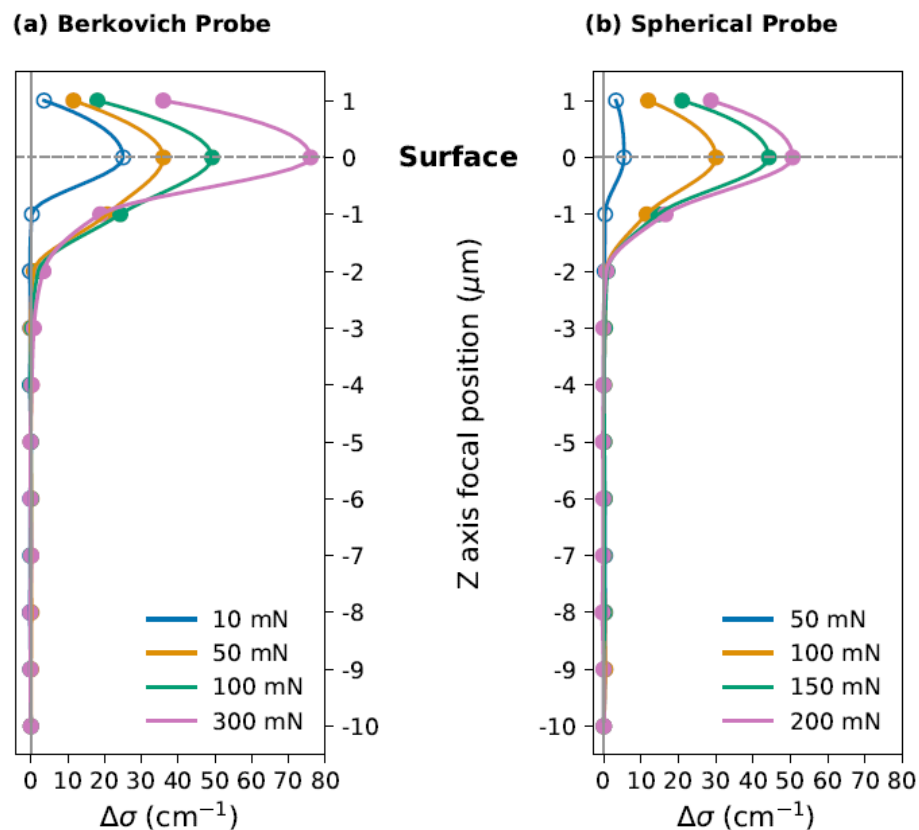


FIG. 2: Z profiles collected with the NA 0.95 objective at imprints that were generated with (a) a Berkovich probe and (b) a spherical probe at various indentation loads (as indicated). The Z profiles were determined from Raman spectra collected in the center of the imprint with the focal plane being shifted stepwise along the z axis starting 1 μm above the surface ($z = 1 \mu\text{m}$) and ending 10 μm into the bulk of the specimen bulk ($z = -10 \mu\text{m}$). The dotted line indicates the position of the surface ‘S’. The thin grey line indicates the relative shift $\Delta\sigma = 0 \text{ cm}^{-1}$ for the unperturbed bulk specimen.

3.2 Mapping experiments on high-load Berkovich and spherical imprints

The spectral data collected with the NA 0.5 and NA 0.95 objectives in the Raman mapping experiments were converted into 10 μm x 10 μm images depicting spatial changes of the relative shift $\Delta\sigma$ in the indented glass regions. Raman mapping experiments were conducted at three different indents per indentation load with each objective. Non-zero values of $\Delta\sigma$ indicated deformation-induced deviations from the pristine glass structure (due to densification). The larger the relative shift the more severe the underlying deformation (densification) of the glass structure can be assumed to be.

Figures 3a and 3b show as examples the Raman images obtained with the NA 0.95 and NA 0.5 objectives of the same residual indent generated at 300 mN with the Berkovich probe. In both images, the region of non-zero $\Delta\sigma$ values outlined the triangular shape for the Berkovich imprint replicating the anisotropic

geometry of the indenter probe. Within the triangular region, the relative shift was not homogeneous over the imprint area, but regions of varying magnitudes can be distinguished. In the map collected with the NA 0.95 objective, a threefold symmetry can be identified with the larger shift located in those regions of the indented material that were in contact with the edges of the Berkovich probe. The largest $\Delta\sigma$ values were localized in the center of the imprint. No such symmetry pattern was discernible in the image collected with the NA 0.5 objective of the Berkovich imprint. However, with the spectral shift being an order of magnitude smaller than that measured with the NA 0.95 objective, it is reasonable to expect that finer features in the image might not be resolved. The area where the largest $\Delta\sigma$ values were recorded was moved somewhat away from the imprint center and appeared to be larger than in the NA 0.95 map. A similar off-center location of the largest (MB) shifts was observed in the Raman map of a 490 mN-Vickers imprint in [19]. However, it is suspected that a non-optimized spectroscopy setup can be blamed for the distorted shift distribution in both cases (will be discussed later).

Figures 3c and 3d depict a comparable set of Raman images obtained with the NA 0.95 and NA 0.5 objectives for a 200 mN imprint made with the spherical probe, respectively. The mapped residual appears to be of slightly non-circular shape. Its elliptical distortion was most likely caused by a marginal misalignment between the indentation axis and sample surface. In both Raman images, the region of non-zero $\Delta\sigma$ values consisted of iso-magnitude rings which were concentrically arranged around the highest shift values in the center of the imprint. The shift magnitude of the rings decreased towards the rim of the imprint. However, the magnitude of the $\Delta\sigma$ values recorded with the NA 0.5 objective are again an order of magnitude smaller than those recorded with the NA 0.95 objective.

Figures 4a and 4b show maps of density changes in and around the residual Berkovich imprint based on the empirical correlations with the $\Delta\sigma$ and D_2 shifts (see section S1, Tab. S2, Supplemental Material).

The imprint area exhibited, in general, an increased density compared to the surrounding unperturbed bulk. Further, a threefold symmetrical pattern similar to the one in the $\Delta\sigma$ map can also be recognized in the densification map. The densification was slightly more pronounced along the edges of the indenter probe, where more intense densification-inducing shear stresses are usually generated than on the facets of the probe.[12,73,74] The largest densification was seen in the center of the residual imprint. The densification values appeared to decrease towards the rim of the imprint. These observations were in line with previous Raman scanning experiments conducted on (portions of) residual Vickers indents generated at significantly higher loads.[12,20,63] The largest increase in relative density found in the maps of the analyzed Berkovich imprint was +16.3 % ($\Delta\sigma$ shift) respective +18.1 % (D_2 shift) dependent upon which parameter correlation was used for the densification estimate.

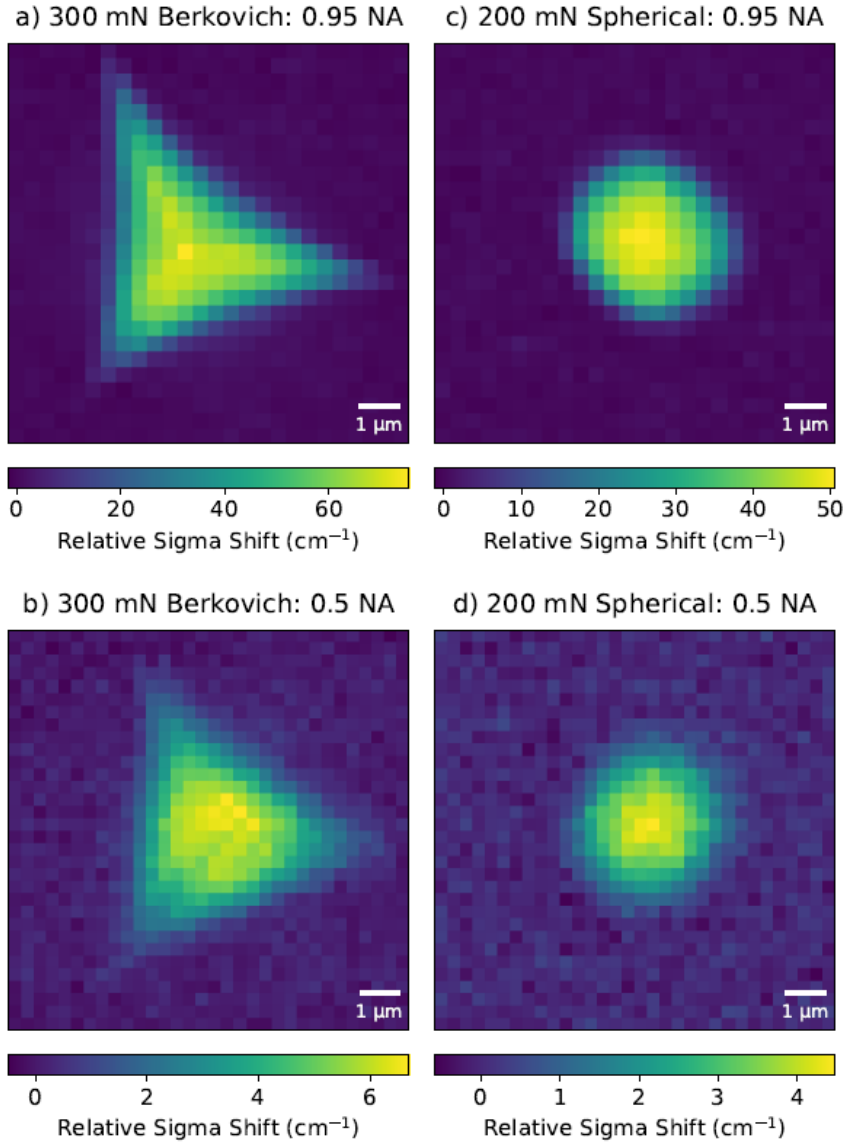


FIG. 3: Raman images (10 μm x 10 μm) showing the relative shift $\Delta\sigma$ distribution of residual Berkovich and spherical imprints. The images 3(a) and (b) were obtained from a 300 mN Berkovich imprint in Raman mapping experiments conducted with the NA 0.95 objective and NA 0.5 objective, respectively. The 3(c) and (d) were created from spectral data collected with the NA 0.95 and NA 0.5 objectives on a 200 mN spherical imprint, respectively. At diffraction limit and for $n=1$: NA 0.95: LD = 0.68 μm, DOF = 1.30 μm; NA 0.5 objectives: DOF = 2.36 μm, DOF = 8.51 μm.

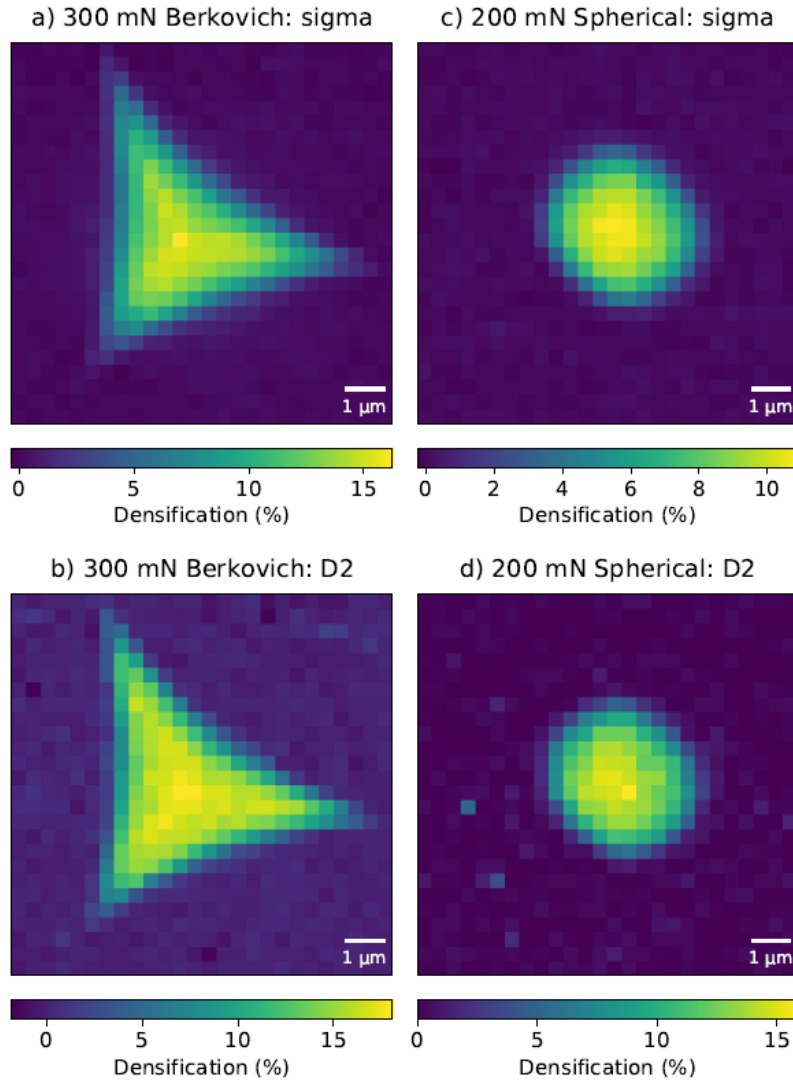


FIG. 4: Raman images ($10\ \mu\text{m} \times 10\ \mu\text{m}$) showing density changes in residual Berkovich and spherical imprints determined in Raman measurements with the NA 0.95 objective. The densification maps for the 300 mN Berkovich imprint were obtained from empirical relations based on (a) the $\Delta\sigma$ and (b) the D_2 shifts. The densification maps for the 200 mN spherical imprint were obtained from empirical relations based on (c) the $\Delta\sigma$ and (d) the D_2 shifts. At diffraction limit and for $n=1$: NA 0.95: LD = $0.68\ \mu\text{m}$, DOF = $1.30\ \mu\text{m}$; NA 0.5 objectives: DOF = $2.36\ \mu\text{m}$, DOF = $8.51\ \mu\text{m}$.

Recent Raman microprobing experiments determined relative density increases of up to +18.4 % based on the $\Delta\sigma$ shift measured in residual Vickers imprints generated at indentation loads $> 5\ \text{N}$. [11] The largest changes in density (based on D_2 shifts) were reported as +16 % (19.62 N indent), +17.4 % (2.94 N indent) or +20 % (500 mN indent) in Raman scanning experiments on residual Vickers indents. [12,20,63] Refractive index measurements determined a maximum density change of +16 % for a residual Vickers

indent generated at 2.94 N.[75] The reported values are below the densification saturation value of 21 % achieved in DAC compression tests on FS.[71,76] However, it has been suggested that the degree of densification during indentation is restricted by the maximum hydrostatic pressure generated under the indenter probe.[11] As such, a maximum increase in density of FS is limited to around 18 % for the Berkovich/Vickers geometry.[11]

Figures 4c and 4d show maps of the densification level of the residual spherical imprint estimates from the correlation with the $\Delta\sigma$ and D_2 shifts (see section S1, Tab. S2, Supplemental Material), respectively. The densification values were highest in the center region of the imprint. This was expected since the main compressive stress occurs along the axis of applied load during indentation with a spherical indenter probe.[75,76] The densification levels diminished when moving from the center towards the rim. The largest density changes seen in the residual spherical imprint were about +10.9 % ($\Delta\sigma$ shift) to +15.9 % (D_2 shift) and as such appeared to be below the maximum densification achievable in Berkovich/Vickers indentations. Another study that quantitatively analyzed the density changes in spherical imprints in FS extracted density information from the fictive temperature determined by FTIR (Fourier Transform Infrared) spectroscopy.[77] In that study, macroscopic imprints were produced by pressing steel balls of diameters of 1.6 mm and 3.2 mm at loads between 588 N and 1471 N into a FS sample. Only marginal density changes (< +1 %) were observed in the center region of the macroscopic imprints which was explained by the authors as being partly due to the low contact pressures (≤ 6 GPa) employed during indentation.

4 Discussion

To collect meaningful spectroscopic information from the small deformation zone of indented glasses, obfuscations of the Raman measurements by spectral contributions from the unperturbed specimen bulk must be minimized (or eliminated). As such, considerations of the dimensional correlation between the spatial resolution (analysis volume) of the Raman measurement and the size of the deformation zone generated in the indentation are critical.[11,13,33,36] A mismatch between analysis volume and deformation volume may result in an inaccurate depiction of the actual spectral and deduced structural changes induced during indentation as has been recently shown in in-situ spectroscopic measurements on FS.[33,36]

In place of analysis volume and deformation volume, the authors will refer to their 2-D representations (analysis area and densification-zone thickness) to be in line with the schematic illustrations used for discussing the results of the present study. In the following paragraphs, the process for estimating these 2-D parameters will be detailed.

4.1 Estimation of thicknesses of densification zones generated in indentations

During indentation-induced deformation of fused silica, densification is believed to account for 85 % to 92 % of the total indentation volume.[1,80] Hence, a large portion of the deformation zone adjacent to the residual imprint is comprised of densified material, the extent of which can be estimated by various approaches:

For indenter probes with a cone-equivalent angle of $\varphi = 70.3^\circ$ (Vickers, Berkovich), Rouxel *et al.* [1] suggested the following equation based the Boussinesq's elastic stress field:

$$z_{d,i} = [F \cdot (1 + \nu)/(3\pi p_0)]^{1/2} \quad (1)$$

where $z_{d,i}$ is the thickness of the densification zone extending from the apex of the residual imprint, F is the indentation force, ν is the Poisson's ratio ($\nu = 0.252$ for densified FS) and p_0 is the pressure at the onset of densification ($p_0 = 8$ GPa for FS).

Based on chemical dissolution experiments, Guin *et al.* [14] determined the empirical relationship:

$$z_{d,i} \approx 1.88 \cdot h_{max} \quad (2)$$

linking $z_{d,i}$ with the maximum indentation depth h_{max} for Berkovich indentations.

Mound observed that the diameter of the densified zone ($= 2 \cdot z_{d,s}$) equals the width of the imprint measured edge to edge across the imprint center for indentations with any three-sided pyramidal probe (with a centerline-to-face angle between 45° to 65°).[81] For Berkovich indentations in particular, it was suggested:

$$z_{d,s} = 3.8 \cdot h_r \quad (3)$$

whereby $z_{d,s}$, refers to the thickness of the densified zone measured from the surface.[81] The parameter $z_{d,s}$ is related to $z_{d,i}$ via $z_{d,s} = z_{d,i} + h_r$ with h_r being the residual depth of the imprint. Furthermore, the authors of this study analyzed previously published cross-sections of residual Vickers imprints generated at indentation forces ranging from 2 N to 30 N reported in [25-28] and found the following empirical relationship (see section S2, Supplemental Material):

$$z_{d,s} = 2.8 \cdot h_r \quad (4)$$

For spherical indentations, $z_{d,s}$ might be estimated based on microscopic observations using

$$\Delta V/V \approx h_r/z_{d,s} \quad (5)$$

with $\Delta V/V$ representing the compressibility of the glass.[82] The authors assumed the compressibility to be equal to the densification ratio achievable during indentation of FS ($\Delta V/V = 0.18$).

Thickness estimates for densified zones together with relevant indentation dimensions (h_r , h_{max}) are summarized in Tab. 1 for the various imprints analyzed in this study. It should be pointed out again, that the densified zone around indentations consists of heterogeneously densified material. Besides variations in the plane perpendicular to the indentation axis (see mapping experiments), the densification also changes

along the indentation axis (z axis) with the density being at the highest just under the tip and decreasing with increasing distance from the tip.[9,12,74,83]

4.2 Effect of analysis area on spectral measurements

Z profile measurements on high-load spherical imprints

First insights on the effect of the NA value on the performance of the microscope objective in Raman measurements were gained from the Z profile experiments conducted on the 200 mN spherical imprints (see section 3.1). Figures 5a and 5b illustrate some of the steps of the Z profile experiments conducted with the NA 0.5 and NA 0.95 objectives, respectively by depicting their analysis areas ($= LD \cdot DOF$, see section 2.2) at various focal positions in relation to the densification zone of the residual imprint. The outlines for the spherical imprint and densification zone were based on the dimensional parameters given in Tab.1.

As shown in Fig. 5a, the analysis area of the NA 0.5 objective extended across the densification zone and into the adjacent specimen bulk even at focal positions in the surface-near region ($z \geq -1 \mu\text{m}$). Diluted by spectral contribution from unperturbed material, the densification-related spectral changes (e.g., MB shift) were thus significantly less pronounced in the Raman spectra collected with this objective than with the high-NA objective (see Figs. 1b and 1c). Due to the large DOF, the absolute amount of densified material covered by the analysis area remained initially unchanged for focal positions deep into the specimen bulk. Only when moving the focal plane to $z \leq -5 \mu\text{m}$, the analysis area covered less and less of the densification zone until it was comprised of unperturbed material only (Fig. 5a). However, the ratio of densified material to unperturbed material within the analysis area continuously decreased, when shifting the focal plane of the objective away from the surface. The downwards-sloping linear shape of the Z profile of the NA 0.5 objective seen in Fig. 1a was a result of this gradual weakening of the densification-related spectral alterations ($\Delta\sigma \rightarrow 0$) relative to the Raman signal of the unperturbed material.

The intercept of the Z profile at $\Delta\sigma = 0$ marked the focal position where the share of densified FS within the analysis area has declined to such a degree that its spectral contribution could no longer be detected. An intercept location of about $9 \mu\text{m}$ indicated the detection of spectral contributions from densified material far beyond the estimated physical extent of the densification zone for that residual imprint (see Tab.1).

On the other hand, the NA 0.95 objective collected spectral information originating (mostly) from the densification zone when focused in the near-surface region due to its considerably smaller analysis area (Fig. 5b). At focal position $z = 0 \mu\text{m}$, the analysis area included the upper parts of densification zone where the highest degree of densification could be expected.[11,12,83] Indeed, the most pronounced spectral changes associated with densification, hence, the largest $\Delta\sigma$ shift were seen in the spectra collected at $z = 0 \mu\text{m}$ (see Fig. 1b). At $z = -1 \mu\text{m}$, analysis area extended into the lower regions of the densification zone containing material densified to a lesser degree and might have even skirted the elastically deformed region adjacent to the densification zone. The associated Raman spectrum exhibited smaller densification-related

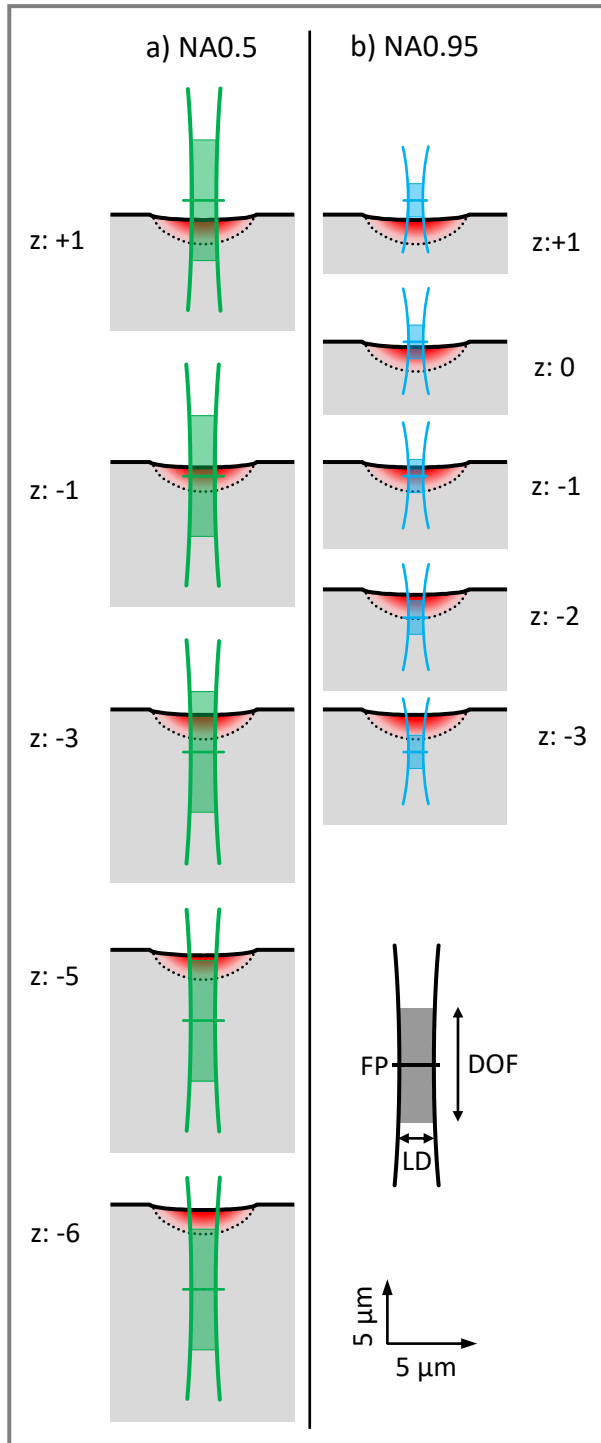


FIG. 5: Illustration of the outline of densification zone of a 200 mN spherical imprint in relation to idealized analysis areas of the (a) NA 0.5 and (b) NA 0.95 objectives. The lateral spot diameter (LD) and depth of field (DOF) are shown with the focal plane (FP) of the objective being shifted to various z positions (in μm) as indicated. The dotted line marks the extent of the densification zone.

spectral alterations and, thus, a smaller $\Delta\sigma$ shift than at $z = 0 \mu\text{m}$. The spectral changes and the corresponding $\Delta\sigma$ shift were even further diminished in the Raman profile collected at $z = -2 \mu\text{m}$. There, a large portion of the analysis area extended into the specimen bulk and spectral contribution of the unperturbed material primarily shaped the Raman profile. For focal position beyond $z = -2 \mu\text{m}$, the analysis area appeared to contain (almost) exclusively unperturbed material and, thus, no spectral contributions of the densification zone were detected ($\Delta\sigma = 0$). As a consequence, the shape of the Z profile for the NA 0.95 objective is as shown in Fig. 1a.

Based on the intercept position of the Z profile, the densification zone was estimated to extend about $2.5 \mu\text{m}$ from the surface into the specimen bulk which was in good agreement with the thickness values of about $2.1 \mu\text{m}$ (Tab. 1). As such, the spectral data collected with NA 0.95 objective represented the degree of the densification and the lateral dimension of the densification zone much more accurately than was possible with the NA 0.5 objective.

Raman mapping of high-load Berkovich and spherical imprints

Further, more visual evidence for this conclusion was gathered by Raman imaging of residual imprints (see section 3.2). Figures 6a and 6b pictured the analysis area of the NA 0.5 and NA 0.95 objectives in relation to the densification zone of a 300 mN Berkovich imprint and a 200 mN spherical imprint, respectively. (The dimensional parameters for the residuals and densification zones are summarized in Tab. 1.)

The analysis areas are shown at a focal position of $z = 0 \mu\text{m}$ at which all Raman imaging was conducted in this study. The outlines for the residuals and their densification zones were based on the dimensional parameters given in Tab.1. At first glance the lateral resolution for both objectives appears to be adequate for mapping these larger imprints, as the LD of both optical configurations was smaller than the lateral dimension of the residual imprints. However, the two objectives differed more substantially in their DOF and, thus, its effect on the extent of the analysis area was considered more critical in assessing the suitability of the two microscope objectives for Raman imaging of indented glasses.

As for the 200 mN spherical imprint (discussed earlier), the analysis area of the NA 0.5 objective extended much deeper into the sample than for the NA 0.95 objective and presumably beyond the densification zone of the Berkovich imprint. Thereby, the NA 0.5 objective simultaneously collected spectral information from densification zone as well as large portions of marginally affected (elastically deformed) material adjacent to the densification zone and pristine glass farther into the sample bulk.

Consequently, the Raman spectra obtained with the NA 0.5 objective for both imprints showed densification-related spectral changes only in diminished form (e.g., smaller band shifts, see Fig. 3) leading to significantly smaller increases in relative density than in the maps collected with the NA 0.95 objective (see Fig. 4). Additionally, the inferior volume and spatial resolution of the lower-numerical aperture objective resulted in the less focused appearance of the spectral images, impeding the distinction of

symmetry patterns in the parameter distribution in the maps obtained with the NA 0.5 objective (see Figs. 3 and 4). The more confined analysis area of the NA 0.95 objective ensured a more accurate representations of the indentation-induced spectral and relative density changes, as the collected spectral information appeared to originate predominantly from the densification zones of both imprint geometries shown in Figs. 6a and 6b.

4.3 Effect of size of densification zone on spectral measurements

Z profile measurements on Berkovich imprints generated at different loads

The maximum hydrostatic pressure generated during an indentation equals the hardness of the indented material. In this context, the relevant parameter to be considered is the Meyer hardness $H_M = F/A$, where F is the applied indentation force and A is the projected area of the impression. For fused silica, H_M was determined to be about 9 GPa in the indentations conducted in this study and in agreement with other publications.[33,36] The indentation-induced shear strain can be estimated with

$$\varepsilon_I = 0.2 \cdot h_c/a \quad (6)$$

where h_c is the contact depth and a is the contact radius of the indent.[85]

For pyramidal probes, $h_c/a \approx 1/\tan\varphi$, where 2φ is the effective included angle of the equivalent conical indenter. Since $\varphi \approx 70.3^\circ$ for probes of Berkovich geometry, the shear strain generated by such probes can be assumed to be $\varepsilon \approx 0.072$. As the induced shear strain is pre-determined by the indenter angle and the hydrostatic pressure by the material's hardness, the intensity of the stress field in Berkovich indentations is load invariant (for plastic indents free of cracking). Therefore, the indentation-induced densification and associated spectral response was expected to be uniform across the applied indentation forces.

However, the maxima of the densification-related $\Delta\sigma$ shift (observed at $z = 0 \mu\text{m}$) varied quite significantly between the indentation forces (Fig. 2a). The cause for this perceived discrepancy is schematically illustrated in Figs. 6a and 6c. The figures provide a comparison between the dimensions of the densification zones generated at different indentation forces with the Berkovich probe and the analysis area of the NA 0.95 objective used in the Z profile measurements on these imprints. The range of the analysis area was indicated for different locations along the z axis. As can be seen, the dimensions of the residual Berkovich imprints and their associated densification zones became smaller with decreasing indentation forces. Thus, the amount of the densification zone contained within the analysis area changed with the indentation force: For the 300 mN imprint, the analysis area covered the upper region of the densification zone associated with highest degree of densification, hence, the largest $\Delta\sigma$ shift was recorded. For the 100 mN imprint, the analysis area extended into regions of less perturbed (or even unperturbed) material and smaller $\Delta\sigma$ values were measured. As the indentation force was reduced to 50 mN and 10 mN, the amount of unperturbed material contained within the analysis area grew. With that, the densification-related spectral alterations

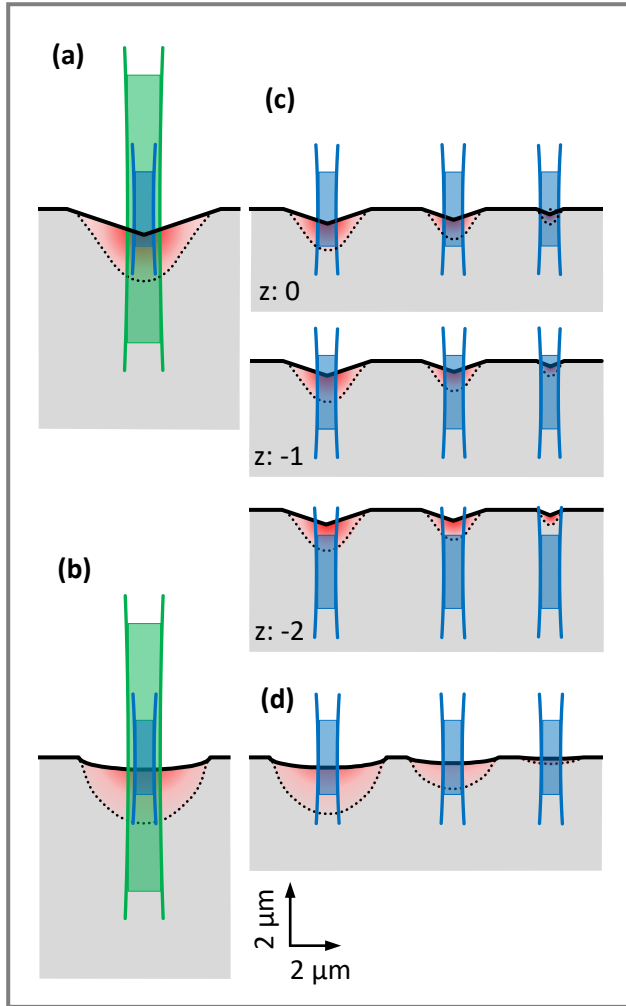


FIG. 6: Dimensional correlation between idealized analysis area of microscope objective and densification zone of various residual imprints. Figs. 6(a) and 6(b) shows the analysis areas of the NA 0.5 and NA 0.95 objectives at $z = 0 \mu\text{m}$ in relation to the densification zones of the 300 mN Berkovich and the 200 mN spherical imprints, respectively. The analysis areas were shown at the focal position $z = 0 \mu\text{m}$ and were outlined in green and blue for the NA 0.5 and NA 0.95 objective, respectively. Fig. 6(c) shows the analysis area for the high-NA objective for residuals generated in indentations with the Berkovich probe at 100 mN, 50 mN and 10 mN (from left to right). The analysis area was shown for the focal positions at $z = 0 \mu\text{m}$, $-1 \mu\text{m}$ and $-2 \mu\text{m}$ as indicated. Fig. 6(d) shows the analysis area at $z = 0 \mu\text{m}$ for the high-NA objective for residuals generated in indentations with the spherical probe at 150 mN, 100 mN and 50 mN (from left to right).

were increasingly obfuscated by the spectral contribution of unperturbed material. As a consequence, significantly smaller $\Delta\sigma$ shifts were measured than should be expected based on indentation-induced stresses. Therefore, the apparent variation in the $\Delta\sigma$ -shift maxima observed between Berkovich imprints

generated at different loads is caused by the dimensional mismatch of densification zone and analysis area. In light of this observation, the perceived load-dependencies of the spectral shift or degree of densification that were reported in some of the earlier Raman studies on glasses indented with Vickers probes [16,19,75,86], that also have a self-similar geometry, may need to be re-evaluated.

Naturally, the portion of densified material contained within the analysis area steadily decreased for all Berkovich imprints, when moving the focal position farther into the sample bulk (see Fig. 2a). Consequently, the $\Delta\sigma$ shift rapidly declined with increasing distance from the surface until the spectral signal from the densification zone was no longer detectable ($\Delta\sigma = 0$). Obviously, this occurred at focal positions closer to the surface for low-force imprints due to the smaller size of their densification zones. To illustrate this point, the extent of the analysis area in relation to the densification zone for the focal positions $z = -1 \mu\text{m}$ and $z = -2 \mu\text{m}$ was also indicated in Fig. 6b.

From the profile curves in Fig. 2a, the following intercept positions were determined for the various loads: $< 1 \mu\text{m}$ (10 mN), $2.1 \mu\text{m}$ for (50 mN), $2.5 \mu\text{m}$ (100 mN) and $3 \mu\text{m}$ (300 mN). There were too few data points for the 10 mN imprint to determine the intercept more precisely. As mentioned earlier, the intercept positions may be used as a measure for the thickness of the densification zone if the DOF is sufficiently small. As such, the thickness value obtained from the Z profile for a particular load was within the range of thickness estimates given for the corresponding Berkovich indentation in Tab.1, though the Z-profile-based thicknesses were skewed towards the upper margins listed in the table for forces $< 300 \text{ mN}$.

Z profile measurements on spherical imprints generated at different loads

Unlike in the case of Berkovich indentations, the strain induced by the spherical probe is dependent on the applied indentation force. Values for ε_1 were estimated to range from 0.038 to 0.058 (eqn. 6) between the highest and lowest indentation force applied to the spherical probe in this study. Mantsi *et al.* [2] simulated the plastic response of a model material emulating silica glass under combined loading of hydrostatic pressure and shear (as may occur during indentation). As result, they produced a quantitative map (Fig. 2 in [2]) that charts the distribution of residual volumetric strain (densification) and residual shear strain as isodensity and isoshear-isostress lines as function of hydrostatic pressure and shear stress. Using this map, the densification level at a particular indentation force was estimated by assuming it is equal to the value of the isodensity line at the intersection of the isostrain line (with a value equal to ε_1 at that force) and the hydrostatic-pressure vertical at 9 GPa (H_M for FS). Based on these estimates, the difference in densification levels between applied indentation forces amounted to be only 3%, which would translate to a variation of about 14 cm^{-1} in the $\Delta\sigma$ parameter. However, a comparison of the $\Delta\sigma$ maxima measured in the Z-profiles (at $z = 0 \mu\text{m}$) for various spherical imprints showed a clear divergence from that range for the imprints at

100 mN and 50 mN (see Fig. 2b). This discrepancy was caused by the mismatch between analysis area and densification-zone thickness as illustrated in Fig. 6d.

The figure shows the dimensions of the densification zones generated at indentation forces from 50 mN to 150 mN with the spherical probe in relation to analysis area of the NA 0.95 objective used in the Z profile measurements on these imprints. A companion illustration for the 200 mN spherical imprint can be found in Fig. 6b. As can be seen, the analysis area extended beyond the boundaries of the densification zones into the sample bulk for the two smallest loads. Here, the Raman spectra collected in the surface near regions were (significantly) diluted by the spectral contribution from the unperturbed bulk and weaker than expected densification-related spectral changes were measured. This effect was most pronounced for the lowest indentation force due the significantly thinner densification zone compared to the spherical imprints generated at higher loads.

The Z profiles collected on all the spherical imprints exhibited a similar curved shape that was previously discussed for the 200 mN spherical imprint in section 4.3. Based on intercept positions of the Z profiles, the vertical extent of the densification zone was estimated to be $< 1 \mu\text{m}$ for the 50 mN imprint and about $2 \mu\text{m}$ for the imprints generated at higher forces. The Z profile-based values were comparable with the thickness estimates given in Tab.1 for the two highest loads. However, the value for 100 mN was significantly larger than the estimate in Tab. 1. This indicates that the densification zone was detected beyond its actual physical extent due to the dimensional mismatch between the analysis area of the NA 0.95 objective and the densification zone of small spherical imprints (generated at indentation forces $< 150 \text{ mN}$).

4.4 Variation in spectral response observed for spherical and Berkovich imprints

In the Raman mapping experiments, overall lower changes in density were seen in the images collected on the spherical imprint than in those of the Berkovich imprint (see Fig. 4). As discussed earlier, the spectral information obtained during mapping of high-load (large) residuals originated predominantly from the densification zone. That implies that the variation in the maximum increase in density did not constitute a measurement artifact (due to an oversized analysis area) but might be explained by differences in the strains induced by the two probe geometries. Indeed, the aforementioned plastic response model [2] predicted a higher densification during indentation with the Berkovich probe than with the spherical probe based on the associated indentation strain and contact pressure. However, the predicted increases in density (by 18 % for Berkovich imprint and by 16 % for spherical imprint) were more in line with the densification maxima obtained from the D_2 shift than the generally lower trending $\Delta\sigma$ -based values (see section 3.2).

4.5 Assessing the veracity of the spectral response

As discussed earlier, the actual spectral response in residual imprints generated by probes with self-similar geometry should be invariant to the applied indentation force as the generated stress field causing the

underlying structural changes in the glass is invariant. However, the observed spectral response is heavily influenced by how well the load-dependent size of the densification zone matches the analysis area. One way to verify a suitable match between those dimensional parameters is to track indentation-induced quantifiable spectral changes to the Raman profile (e.g. shifts in peak positions) between differently sized residual imprints that were generated at different indentation forces with the same probe in the glass specimen.[33,36]

Replicating this approach, the relative shift $\Delta\sigma$ for various Berkovich imprints studied in this paper with the NA 0.95 objective was plotted in Fig. 7. Also, data from a recently published Raman study on Vickers imprints[11] were added to Fig.7 to further illustrate the importance of optimizing the optical setup for Raman measurements on indented glasses.

The Vickers imprints were generated at indentation forces ranging from 300 mN to 10 N and analyzed with two microscope objectives differing in the numerical aperture (NA 0.75, NA 0.9).[11] The plotted $\Delta\sigma$ values correspond to the largest shifts observed for each indentation load in the Z profile measurements conducted in both studies. For the Berkovich imprints analyzed in this study, the relevant $\Delta\sigma$ -force data can be found in Tab. 1. The corresponding data extracted for the Vickers imprints from [11] are summarized in Tab. S4 (Supplemental Materials, section S3).

In all three data sets, the $\Delta\sigma$ magnitude initially increased with the applied indentation force, as the deformation zone and associated densification zone of the generated imprint grew and the portion of the analysis area containing densified material expanded. However, the $\Delta\sigma$ magnitude eventually maintained a constant value (with increasing indentation force) once the analysis area contains predominantly densified material. As such, the $\Delta\sigma$ -force data were well characterized by an asymptotic fit ($y = a(1 - c^x)$) which was displayed as a dashed line for the average values of each data set in Fig.7. In these fits, the asymptote value marked the true $\Delta\sigma_i$ shift inherent to the (maximum) structural/spectral changes in the glass induced during indentation and undiluted by spectral contributions from unperturbed bulk. The shaded area indicates the data spread within each set, which means the average value \pm standard deviation for the Vickers imprints and measured value \pm uncertainty for the Berkovich imprints.

Furthermore, the fit allowed to ascertain a minimum indentation force that satisfy the matching condition (densification zone \geq analysis area) for reliable and true Raman measurements on indented glasses and which experimental implications were illustrated by the Vickers data sets: As expected, the fits of the two Vickers data sets converged onto the same asymptotic value of about $91 \pm 2 \text{ cm}^{-1}$, as the same set of Vickers imprints were analyzed by both objectives. However, the minimum force values (= lowest force at which was first $\Delta\sigma_i$ observed) were quite different for the two microscope objectives: $F_{\text{Vick,NA0.75}} \approx 9 \text{ N}$ and $F_{\text{Vick,NA0.9}} \approx 3.5 \text{ N}$. It means much higher forces were required to generate imprints (densification zones) large enough to ensure a dimensional match with the more expansive analysis area of the low-aperture

objective for inherent shift measurements. Moreover, it exemplifies the intercorrelation between indentation parameters and the optical setup that need to be considered for optimizing Raman spectroscopic measurements on indented glasses.

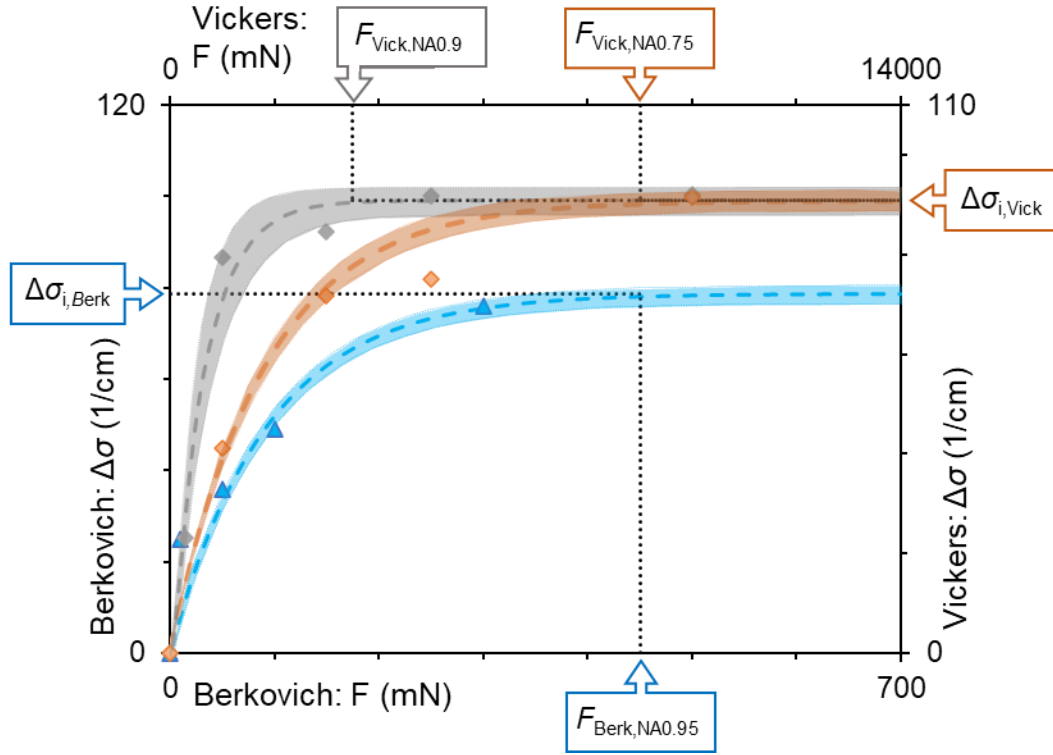


FIG. 7: Relative shift $\Delta\sigma$ measured in residual FS imprints generated at different indentation forces F . Three data sets (symbols) are presented: data collected with the NA 0.95 objective on the Berkovich imprints in this study (triangles); data collected with a NA 0.75 (orange diamonds) and NA 0.9 (grey diamonds) objectives on Vickers imprints from ref. [11]. The asymptotic fits of the average values of the individual data sets are indicated as dashed lines. The shaded area indicates the data spread within each set. The fitted asymptote values are marked as inherent shifts $\Delta\sigma_{i,Berk}$ and $\Delta\sigma_{i,Vick}$ for the Berkovich and Vickers imprints, respectively. The minimum indentation force at which the inherent shifts could be observed was marked for each data set accordingly ($F_{Berk,NA0.95}$, $F_{Vick,NA0.9}$ OR $F_{Vick,NA0.75}$).

For the Berkovich imprints analyzed in this study, the inherent shift was determined to be $\Delta\sigma_{i,Berk} = (77 \pm 2) \text{ cm}^{-1}$. The largest relative shift $\Delta\sigma = (76 \pm 2) \text{ cm}^{-1}$ measured for the 300 mN-Berkovich imprints was within the range of the inherent value. From which, it can be conclude that the indentation force was sufficiently close to the minimum $F_{Berk,NA0.95} \approx 450 \text{ mN}$ (estimated from the data plot) for an adequate match between analysis area and densification-zone size. This finding also demonstrates that reliable and

meaningful Raman spectroscopic microprobing and imaging of sub-newton imprints in glasses is possible with an optimized optical configuration and suitably matched indentation parameters. Sub-newton imprints usually exhibit fewer cracks or no cracking at all, which reduces or eliminates the aforementioned issues associated with cracking in the interpretation of the spectral data collected on indented glasses (see Introduction).

As seen in Fig. 7, the inherent shifts determined for the Vickers and Berkovich data sets were noticeably different which might seem to challenge the expectation that probes with equal-cone geometries (like Vickers and Berkovich) induce similar densification levels in fused silica.[11] However, the direct comparison of Raman data collected at different laboratories is difficult, as the measurement and analysis of spectral data on glasses are quite sensitive to:

- disparities in the material properties in the initial (unperturbed state) of the investigate glass specimen (e.g. OH content, fictive temperature)[72]
- differences in the experimental configuration used for the Raman spectroscopic measurements (such as polarization, use of notch or edge filters, choice of microscope objective, spectral resolution)[72,33,36]
- deviations in resulting quality of the collected spectral data (e.g. signal-to-noise ratio),
- variations in post-collection data processing (e.g. handling of the baseline correction).

For example, the base value σ_0 , that characterized the unperturbed state of the FS and was used to calculate the relative shift $\Delta\sigma$ in Fig. 7, varied widely between the study conducted on the Vickers imprints (398 cm^{-1})[11], our work on Berkovich imprints (412 cm^{-1}) and other Raman studies on FS specimen: 404 cm^{-1} ,[86] 419 cm^{-1} ,[37] 422 cm^{-1} ,[72] and $(415\text{ to }423)\text{ cm}^{-1}$. [33,36]

The described approach might also be employable for a probe with a non-self-similar geometry, for which the indentation strain only gradually changes with load, such as the spherical probe used in this study. However, more experimental work is required to verify this assumption.

5 Conclusions

This study has shown that the optical configuration of the spectroscopic setup and the applied indentation parameters need to be carefully considered during setup, execution, and analysis of spectral measurements on glass imprints to collect spectral data that accurately capture the indentation-induced changes in the glass network. Otherwise, the interpretability of the spectral data collected within the deformation (densification) zone of the residual imprints may be severely limited as:

- the full extent of the actual indentation-induced structural changes is only partially reflected in the collected spectral data causing a systemic underrepresentation of the structural changes induced into the glass network;

- spectral changes might be perceived beyond the actual physical boundaries of the deformation/densification zone leading to overstating the dimensional extent of associated structural changes;
- perceived spectral variation may originate from a mismatched experimental configuration rather than reflect actual differences in the glass structure (degree of densification);
- the magnitude and distribution of spectral shifts and associated density changes (e.g., symmetry, location and/or size of areas of large shifts) might be erroneously depicted, most noticeably in Raman images collected on imprints generated under anisotropic indentation strain fields (Berkovich imprints).

To collect accurate spectral data, the analysis area determined by the Raman spectroscopy setup and the size of densification zone controlled by the indentation parameters (force, probe geometry) must be matched. To ensure the dimensional match, the (theoretical) DOF and the LD of the spectroscopy setup have to be determined based on the numerical aperture of microscope objective and excitation wavelength of employed laser source (see section 4.2) and assessed in relation to the dimensions of the imprints to be studied.

A first check for an unadulterated spectroscopic measurement of the densification zone is the LD being significantly smaller than the lateral dimension of the imprint. Next, it is essential to verify that the $DOF/2$ is smaller than the thickness of the densification zone of the imprint. Information about the thickness of the densification zone of residual imprints can be gained by direct measurement on prepared cross-sections or by simply estimating the thickness of the densification zone, a less time and effort consuming approach which seemed to provide sufficiently reliable results. Examples for estimating the densification-zone thickness for imprints generated with different probe geometries (spherical, pyramidal) were provided with eqns. (1) to (5) in section 4.1. It should be noted that eqn. (1) is adaptable to other glasses (if parameters ν and p_0 are known for the glass), whereas the empirical eqns. (2) to (5) were formulated based on observations on indented fused silica. Even so, the estimates determined with eqns. (2) to (5) could serve as (low-end) reference points for measurements on some other glasses considering that indented FS exhibits shallower densifications zones than, for example, aluminoborosilicate and soda-lime glasses.[73,75]

An experimental approach for determining the minimum force for a dimensional match, that is employable for any glass type and any (self-similar) probe geometry, is to produce series of plastic imprints with the same probe at increasing indentation loads and then to fit the largest relative spectral shifts measured at the various loads to an asymptotic function (see section 4.6). From the fit, the indentation-induced inherent shift of the glass can be determined and the minimum indentation load, at which the inherent shift is observable, can be identified. Knowing these parameters, one can generate imprints at the lowest forces, hence, with the least cracking damage possible or even free of cracking, and still capture the accurate indentation-induced spectral changes in the glass.

However, essential for collecting reliable and accurate spectral data on sub-newton (crack-free) imprints is the optimization of the Raman spectroscopy setup, as shown in this study. The optical components of the employed setup (most importantly: size of confocal aperture of microscope objective) must be carefully chosen in accordance with the optical properties of the glass sample to optimize the performance of the instrument with respect to the analysis area (minimizing LD and DOF while maintaining a reasonable signal-to-noise ratio). In this context, the choice of wavelength might also be considered for (modest) adjustments of the spatial resolution. A tighter analysis area requires a less expansive densification zone/smaller imprints for a dimensional match, meaning a larger probability to generate them at indentation force below the crack threshold. Comparative Z profile measurements with different objectives on the same imprint can be used to distinguish microscope objectives regarding the size of their analysis area based on their sensitivity to detect densification-related spectral changes along the indentation axis, as illustrated in this study and previous work.[33,36]

On a final note, although the optimization of the instrumental (optical) set-up should be a priority, the spatial resolution of Raman imaging can be potentially further improved using super-resolution image restoration. This currently developed methodology relies on the collection of low-resolution images (oversampling) and subsequent deconvolution of different spatial contribution in Raman spectra via imaging processing algorithms.[87-90]

6 Disclaimer

Certain commercial equipment, instruments, or materials are identified in this paper to foster understanding. Such identification does not imply recommendation or endorsement by the National Institute of Standards and Technology, nor does it imply that the materials or equipment identified are necessarily the best available for the purpose.

7 Copyright statement

Official contribution of the National Institute of Standards and Technology; not subject to copyright in the United States.

8 REFERENCES

- [1] T. Rouxel, H. Ji, J.P. Guin, F. Augereau, B. Rufflé, Indentation deformation mechanism in glass: densification versus shear flow, *J. Appl. Phys.* 107 (2010) 094903, 5 pp, <https://doi.org/10.1063/1.3407559>.
- [2] B. Mantsi, G. Kermouche, E. Barthel, A. Tanguy, Impact of pressure on plastic yield in amorphous solids with open structure, *Phys. Rev. E.* 93 (2016) 033001, 7 pp, <https://doi.org/10.1103/PhysRevE.93.033001>.

- [3] G. Molnar, G. Kermouche, E. Barthel, Plastic response of amorphous silicates, from atomistic simulations to experiments - A general constitutive relation, *Mech. Mater.* 114 (2017) 1-8, <https://doi.org/10.1016/j.mechmat.2017.07.002>.
- [4] D. Rodney, A. Tanguy, D. Vandembroucq, Modeling the mechanics of amorphous solids at different length scale and time scale, *Modelling Simul. Mater. Sci. Eng.* 19 (2011) 083001, 49 pp, <https://doi.org/10.1088/0965-0393/19/8/083001>.
- [5] B. Mantsi, A. Tanguy, G. Kermouche, E. Barthel, Atomistic response of a model silica glass under shear and pressure, *Eur. Phys. J. B.* 85 (2012) 304, 13 pp, <https://doi.org/10.1140/epjb/e2012-30317-6>.
- [6] V. Keryvin, J.-X. Meng, S. Gicquel, J.-P. Guin, L. Charleux, J.-C. Sanglebœuf, P. Pilvin, T. Rouxel, G. Le Quilliec, Constitutive modelling of the densification process in silica glass under hydrostatic compression, *Acta Mater.* 62 (2014) 250-7, <https://doi.org/10.1016/j.actamat.2013.07.067>.
- [7] C.L. Rountree, D. Vandembroucq, M. Talamali, E. Bouchaud, S. Roux, Plasticity-Induced Structural Anisotropy of Silica Glass, *Phys. Rev. Lett.* 102 (2009) 195501, 4 pp, <https://doi.org/10.1103/PhysRevLett.102.195501>.
- [8] K. Xin, J.C. Lambropoulos, Densification of Fused Silica: Effects on Nanoindentation, *Proc. SPIE.* 4102 (2000) 112-21, <https://doi.org/10.1117/12.405275>.
- [9] G. Kermouche, E. Barthel, D. Vandembroucq D, Ph. Dubujet, Mechanical modelling of indentation-induced densification in amorphous silica, *Acta Mater.* 56 (2008) 3222-3228, <https://doi.org/10.1016/j.actamat.2008.03.010>.
- [10] V. Keryvin, S. Gicquel, L. Charleux, J.P. Guin, M. Nivard, J.-C. Sanglebœuf, Densification as the Only Mechanism at Stake during Indentation of Silica Glass? *Key Eng. Mater.* 606 (2014) 53-60, <https://doi.org/10.4028/www.scientific.net/KEM.606.53>.
- [11] S. Bruns, T. Uesbeck, S. Fuhrmann, M. Tarragó Aymerich, L. Wondraczek, D. de Ligny, K. Durst, Indentation densification of fused silica assessed by Raman spectroscopy and constitutive finite element analysis, *J. Am. Ceram. Soc.* 103 (2020) 3076-3088, <https://doi.org/10.1111/jace.17024>.
- [12] A. Perriot, D. Vandembroucq, E. Barthel, V. Martinez, L. Grosvalet, Ch. Martinet, B. Champagnon, Raman Microspectroscopic Characterization of Amorphous Silica Plastic Behavior, *J. Am. Ceram. Soc.* 89 (2006) 596-601, <https://doi.org/10.1111/j.1551-2916.2005.00747.x>.
- [13] P. Malchow, K.E. Johanns, D. Möncke, S. Korte-Kerzel, L. Wondraczek, K. Durst, Composition and cooling-rate dependence of plastic deformation, densification, and cracking in sodium borosilicate glasses

during pyramidal indentation, *J. Non-Cryst. Solids* 419 (2015) 97-109, <https://doi.org/10.1016/j.jnoncrsol.2015.03.020>.

[14] J.-P. Guin, V. Keryvin, L. Charleux, K. Han, J.-C. Sanglebœuf, M. Ferry, A chemical dissolution technique for challenging existing constitutive models of the densification process beneath an indentation imprint in amorphous silica, Available from <https://arxiv.org/abs/1601.06492> (accessed January 21, 2022)

[15] G. Kermouche, G. Guillonneau, J. Michler, J. Teisseire, E. Barthel, Perfectly plastic flow in silica glass, *Acta Mater.* 114 (2016) 146-53, <https://doi.org/10.1016/j.actamat.2016.05.027>.

[16] T. Deschamps, C. Martinet, J.L. Bruneel, B. Champagnon, Soda-lime silicate glass under hydrostatic pressure and indentation: a micro-Raman study, *J. Phys: Condens. Matter.* 23 (2011) 035402, 7 pp, <https://doi.org/10.1088/0953-8984/23/3/035402>.

[17] A. Kassir-Bodon, T. Deschamps, C. Martinet, B. Champagnon, Raman Mapping of the Indentation-Induced Densification of a Soda-Lime-Silicate Glass, *Int. J. Appl. Glass. Sci.* 3 (2012) 29-35, <https://doi.org/10.1111/j.2041-1294.2012.00078.x>.

[18] Y. Kato, H. Yamazaki, S. Yoshida, J. Matsuoka, M. Kanzaki, Measurements of density distribution around Vickers indentation on commercial aluminoborosilicate and soda-lime silicate glasses by using micro Raman spectroscopy, *J. Non-Cryst. Solids.* 358 (2012) 3473-3480, <https://doi.org/10.1016/j.jnoncrsol.2012.04.035>.

[19] A. Winterstein-Beckmann, D. Möncke, D. Palles, E.I. Kamitsos, L. Wondraczek, A Raman-spectroscopic study of indentation-induced structural changes in technical alkali-borosilicate glasses with varying silicate network connectivity, *J. Non-Cryst. Solids.* 405 (2014) 196-206, <https://doi.org/10.1016/j.jnoncrsol.2014.09.020>.

[20] O. Benzine, S. Bruns, Z. Pan, K. Durst, L. Wondraczek, Local Deformation of Glasses is Mediated by Rigidity Fluctuation on Nanometer Scale, *Adv. Sci.* 5 (2018) 1800916, 9 pp, <https://doi.org/10.1002/advs.201800916>.

[21] P. Sellappan, T. Rouxel, F. Celarie, E. Becker, P. Houizot, R. Conradt, Composition dependence of indentation deformation and indentation cracking in glass, *Acta Mater.* 61 (2013) 5949-5965, <https://doi.org/10.1016/j.actamat.2013.06.034>.

[22] B. Lawn, R. Wilshaw, Indentation fracture: principles and applications, *J. Mater. Sci.* 10 (1975) 1049-1081, <https://doi.org/10.1007/BF00823224>.

[23] J.T. Hagan, M.V. Swain, The origin of median and lateral cracks around plastic indents in brittle materials, *J. Phys. D: Appl. Phys.* 11 (1978) 2091-2102, <https://doi.org/10.1088/0022-3727/11/15/007>.

- [24] B.A. Mound, G.M. Pharr, Nanoindentation of Fused Quartz at Loads Near the Cracking Threshold, *Exp. Mech.* 59 (2019) 369-380, <https://doi.org/10.1007/s11340-018-00446-3>.
- [25] A. Arora, D.B. Marshall, B.R. Lawn, Indentation deformation/fracture of normal and anomalous glasses, *J. Non-Cryst. Solids* 31 (1979) 415-428, [https://doi.org/10.1016/0022-3093\(79\)90154-6](https://doi.org/10.1016/0022-3093(79)90154-6).
- [26] J.T. Hagan, Cone cracks around Vickers indentations in fused silica glass, *J. Mater. Sci.* 14 (1979) 462-466, <https://doi.org/10.1007/BF00589840>.
- [27] T.M. Gross, Deformation and cracking behavior of glasses indented with diamond tips of various sharpness, *J. Non-Cryst. Solids* 358 (2012) 3445-3452, <https://doi.org/10.1016/j.jnoncrysol.2012.01.052>.
- [28] P. Yao, W. Wei, C. Huang, J. Wang, H. Zhu, T. Kuriyagawa, Indentation Crack Initiation and Ductile to Brittle Transition Behavior of Fused Silica, *Adv. Mater.* 97 (2013) 667-672, <https://doi.org/10.4028/www.scientific.net/AMR.797.667>.
- [29] D.J. Morris, S.B. Myers, R.F. Cook, Sharp probes of varying acuity: Instrumented indentation and fracture behavior, *J. Mater. Res.* 19 (2004) 165-175, <https://doi.org/10.1557/jmr.2004.19.1.165>.
- [30] T. Chudoba, P. Schwaller, R. Rabe, J.-M. Breguet, J. Michler, Comparison of nanoindentation results obtained with Berkovich and cube-corner indenters, *Phil. Mag.* 86 (2006) 5265-5283, <https://doi.org/10.1080/14786430600746424>.
- [31] D.S. Harding, W.C. Oliver, G.M. Pharr, Cracking during nanoindentation and its use in the measurement of fracture toughness, *Mat. Res. Soc. Symp Proc.* 356 (1995) 663-668, <https://doi.org/10.1557/PROC-356-663>.
- [32] C. Li, L. Zhang, L. Sun, S. Yang, C. Wu, X. Long, J. Ding, Z. Jiang, A quantitative analysis of the indentation fracture of fused silica, *J. Am. Ceram. Soc.* 102 (2019) 7264-7277, <https://doi.org/10.1111/jace.16645>.
- [33] Y.B. Gerbig, C.A. Michaels, In-situ Raman spectroscopic measurements of the deformation region in indented glasses, *J. Non-Cryst. Solids* 530 (2020) 119828, 16 pp, <https://doi.org/10.1016/j.jnoncrysol.2019.119828>.
- [34] N.J. Everall, Confocal Raman microscopy: common errors and artefacts, *Analyst* 135 (2010) 2512-2522, <https://doi.org/10.1039/C0AN00371A>.
- [35] M. Havel, P. Colomban, Smart Raman and Rayleigh spectroscopy for the analysis of nanomaterials. *Microscopy and Analysis*, 113 (2006) 13-15.

- [36] Y.B. Gerbig, C.A. Michaels, (2020) In-situ Raman spectra of indented fused silica, National Institute of Standards and Technology 2020, <https://doi.org/10.18434/M32281> (accessed March 18, 2022)
- [37] T. Deschamps, A. Kassir-Bodon, C. Sonnevile, J. Margueritat, C. Martinet, D. de Ligny, A. Mermet, B. Champagnon, Permanent densification of compressed silica glass: a Raman-density calibration curve, *J. Phys: Condens. Matter* 25 (2013) 025402, 4 pp, <https://doi.org/10.1088/0953-8984/25/2/025402>.
- [38] M.N.M. Patnaik, R. Narasimhan, U. Ramamurty, Spherical indentation response of metallic glasses, *Acta Mater.* 52 (2004) 3335-3345, <https://doi.org/10.1016/j.actamat.2004.03.028>.
- [39] A.C. Fischer-Cripps, A. Bendeli, T.J. Bell, J.S. Field, A.K. Jamting, Methods of correction for analysis of depth-sensing indentation test data for spherical indenters, *J. Mater. Res.* 16 (2001) 2244-2250, <https://doi.org/10.1557/JMR.2001.0308>.
- [40] A.C. Fischer-Cripps, Critical review of analysis and interpretation of nanoindentation test data, *Surf. Coat. Technol.* 200 (2006) 4153-4165, <https://doi.org/10.1016/j.surfcoat.2005.03.018>.
- [41] J.G. Swadener, G.M. Pharr, A Methodology for the Calibration of Spherical Indenters, *MRS Proceedings* 594 (1999) 525, 7 pp, <https://doi.org/10.1557/PROC-594-525>.
- [42] J.S. Field, M.V. Swain, A simple predictive model for spherical indentation, *J. Mater. Res.* 8 (1993) 297-306, <https://doi.org/10.1557/JMR.1993.0297>.
- [43] W.C. Oliver, G.M. Pharr, An improved technique for determining hardness and elastic modulus using load and displacement sensing indentation experiments, *J. Mater. Res.* 7 (1992) 1564-1583, <https://doi.org/10.1557/JMR.1992.1564>.
- [44] C.A. Michaels, Y.B. Gerbig, Raman spectroscopic measurements and mapping on sub-newton Berkovich and spherical imprints in fused silica, <https://doi.org/10.18434/mds2-2764> (in preparation).
- [45] G.A. Myers, C.A. Michaels, R.F. Cook, Quantitative mapping of stress heterogeneity in polycrystalline alumina using hyperspectral fluorescence microscopy, *Acta Mater.* 106 (2016) 272-282, <https://doi.org/10.1016/j.actamat.2016.01.020>.
- [46] G.A. Myers, S.S. Hazra, M.P. de Boer, C.A. Michaels, S.J. Stranick, R.P. Koseski, R.F. Cook, F.W. DelRio, Stress mapping of micromachined polycrystalline silicon devices via confocal Raman microscopy, *Appl. Phys. Lett.* 104 (2014) 191908, 5 pp, <https://doi.org/10.1063/1.4878616>.
- [47] A. Kramida, Yu. Ralchenko, J. Reader, NIST ASD Team (2021), NIST Atomic Spectra Database (ver. 5.9), [Online]. Available: <https://physics.nist.gov/asd> [2022, March 4], National Institute of Standards and Technology, Gaithersburg, MD, <https://doi.org/10.18434/T4W30F>.

- [48] P. McMillan, Structural studies of silicate glasses and melts - applications and limitations of Raman spectroscopy, *Am. Mineral.* 69 (1984) 622-644.
- [49] D.D. Goller, R.T. Phillips, I.G. Sayce, Structural relaxation of SiO₂ at elevated temperatures monitored by in situ Raman scattering, *J. Non-Cryst. Solids* 355 (2009) 1747-1754, <https://doi.org/10.1016/j.jnoncrsol.2009.06.018>.
- [50] J. Burgin, C. Guillon, P. Langot, F. Vallee, B. Hehlen, M. Foret, Vibrational modes and local order in permanently densified silica glasses: femtosecond and Raman spectroscopy study, *Phys. Rev. B.* 78 (2008) 184203, 9 pp, <https://doi.org/10.1103/PhysRevB.78.184203>.
- [51] A. Rahmani, M. Benoit, C. Benoit, Signature of small rings in the Raman spectra of normal and compressed amorphous silica: A combined classical and ab initio study, *Phys. Rev. B* 68 (2003) 184202, 12 pp, <https://doi.org/10.1103/PhysRevB.68.184202>.
- [52] F.L. Galeener, Planar rings in glasses, *Solid State Comm.* 44 (1982) 1037-1040, [https://doi.org/10.1016/0038-1098\(82\)90329-5](https://doi.org/10.1016/0038-1098(82)90329-5).
- [53] A. Pasquarello, R. Car, Identification of Raman defect lines as signatures of ring structures in vitreous silica, *Phys. Rev. Lett.* 80 (1998) 5145-5147, <https://doi.org/10.1103/PhysRevLett.80.5145>.
- [54] T.T. To, D. Bougeard, K.S. Smirnov, Molecular dynamics study of the vibrational pattern of ring structures in the Raman spectra of vitreous silica, *J. Raman Spectrosc.* 39 (2008) 1869–1877, <https://doi.org/10.1002/jrs.2052>.
- [55] H. Liu, S.H. Hahn, M. Ren, M. Thiruvillamalai, T.M. Gross, J. Du, A.C.T. van Duin, S.H. Kim, Searching for correlations between vibrational spectral features and structural parameters of silicate glass network, *J. Am. Ceram. Soc.* 103 (2020) 3575-3589. <https://doi.org/10.1111/jace.17036>.
- [56] M. Wilson, P.A. Madden, M. Hemmati, C.A. Angell, Polarization effects, network dynamics, and the infrared spectrum of amorphous SiO₂, *Phys. Rev. Lett.* 77 (1996) 4023-4026, <https://doi.org/10.1103/PhysRevLett.77.4023>.
- [57] S.N. Taraskin, S.R. Elliott, Nature of vibrational excitations in vitreous silica, *Phys. Rev. B* 56 (1997) 8605–8622, <https://doi.org/10.1103/PhysRevB.56.8605>.
- [58] J. Sarntheim, A. Pasquarello, R. Car, Origin of the high-frequency doublet in the vibrational spectrum of vitreous SiO₂, *Science* 275 (1997) 1925–1927, <https://doi.org/10.1126/science.275.5308.1925>.
- [59] K. Januchta, M.M. Smedskjaer, Indentation deformation in oxide glasses: Quantification, structural changes, and relation to cracking, *J. Non-Cryst. Solids: X* 1 (2019) 100007, 20 pp, <https://doi.org/10.1016/j.nocx.2018.100007>.

- [60] K.-I. Nomura, Y.-C. Chen, R.K. Kalia, A. Nakano, P. Vashishta, Defect migration and recombination in nanoindentation of silica glass, *Appl. Phys. Lett.* 99 (2011) 111906, 3 pp, <https://doi.org/10.1063/1.3637052>.
- [61] F. Yuan, L. Huang, Brittle to Ductile Transition in Densified Silica Glass, *Sci. Rep.* 4 (2014) 5035, 8 pp, <https://doi.org/10.1038/srep05035>.
- [62] S. Fuhrmann, G.N.B.M. de Macedo, R. Limbach, C. Krywka, S. Bruns, K. Durst, L. Wondraczek, Indentation-Induced Structural Changes in Vitreous Silica Probed by in-situ Small-Angle X-Ray Scattering, *Front. Mater.* 7 (2020) 173, 11 pp, <https://doi.org/10.3389/fmats.2020.00173>.
- [63] T. Rouxel, Driving force for indentation cracking in glass: composition, pressure and temperature dependence, *Phil. Trans. R. Soc. A* 373 (2015) 20140140, 26 pp, <https://doi.org/10.1098/rsta.2014.0140>.
- [64] R. Sajzew, R. Limbach, L. Wondraczek, Deformation and Fracture of Silica Glass Fiber Under Sharp Wedge-Indentation, *Front. Mater.* 7 (2020) 126, 10 pp, <https://doi.org/10.3389/fmats.2020.00126>.
- [65] H. Sugiura, R. Ikeda, K. Kondo, T. Yamadaya, Densified silica glass after shock compression, *J. Appl. Phys.* 81 (1997) 1651-1655, <https://doi.org/10.1063/1.364021>.
- [66] M. Guerette, M.R. Ackerson, J. Thomas, F. Yuan, E.B. Watson, D. Walker, L. Huang, Structure and Properties of Silica Glass Densified in Cold Compression and Hot Compression, *Sci. Rep.* 5 (2015) 15343, 14 pp, <https://doi.org/10.1038/srep15343>.
- [67] C. Martinet, A. Kassir-Bodon, T. Deschamps, A. Cornet, S. Le Floch, V. Martinez, B. Champagnon, Permanently densified SiO₂ glasses: a structural approach, *J. Phys: Condens. Matter* 27 (2015) 325401, 7 pp, <https://doi.org/10.1088/0953-8984/27/32/325401>.
- [68] A. Cornet, V. Martinez, D. de Ligny, B. Champagnon, C. Martinet, Relaxation processes of densified silica glass, *J. Chem. Phys.* 146 (2017) 094504, 10 pp, <https://doi.org/10.1063/1.4977036>.
- [69] M. Chligui, G. Guimbretière, A. Canizarès, G. Matzen, Y. Vaills, P. Simon, New features in the Raman spectrum of silica: key-points in the improvement on structure knowledge, <https://hal.archives-ouvertes.fr/hal-00520823> (accessed 31 January 2019)
- [70] H. Sugiura, T. Yamadaya, Raman scattering in silica glass in the permanent densification region, *J. Non-Cryst. Solids* 144 (1992) 151-158, [https://doi.org/10.1016/S0022-3093\(05\)80395-3](https://doi.org/10.1016/S0022-3093(05)80395-3).
- [71] T. Rouxel, H. Ji, T. Hammouda, A. Moréac, Poisson's Ratio and the Densification of Glass under High Pressure, *Phys. Rev. Lett.* 100 (2008) 225501, 4 pp, <https://doi.org/10.1103/PhysRevLett.100.225501>.

- [72] M. Guerette, A. Poltorak, Y. Fei, T.A. Strobel, Permanent densification of silica glass for pressure calibration between 9 and 20 GPa at ambient temperature, *High. Press. Res.* 39 (2019) 117-130, <https://doi.org/10.1080/08957959.2019.1580364>.
- [73] H. Ji, V. Keryvin, T. Rouxel, T. Hammouda, Densification of window glass under very high pressure and its relevance to Vickers indentation, *Scripta Mater.* 66 (2006) 1159-1162. <https://doi.org/10.1016/j.scriptamat.2006.08.038>.
- [74] K.R. Gadelrab, F.A. Bonilla, M. Chiesa, Densification modeling of fused silica under nanoindentation, *J. Non-Cryst. Solids.* 358 (2012) 392-398, <https://doi.org/10.1016/j.jnoncrysol.2011.10.011>.
- [75] Y. Sung, S. Yoshida, Y. Kato, C. Kurkjian, Three-dimensional densification measurement of Vickers-indented glass using digital holographic tomographic, *J. Am. Ceram. Soc.* 102 (2019) 5866-5872. <https://doi.org/10.1111/jace.16508>.
- [76] C. Sonnevile, A. Mermet, B. Champagnon, C. Martinet, J. Margueritat, D. de Ligny, T. Deschamps, F. Balima, Progressive transformations of silica glass upon densification, *J. Chem. Phys.* 137 (2012) 124505, 7 pp, <https://doi.org/10.1063/1.4754601>.
- [77] K. Asai, S. Yoshida, A. Yamada, J. Matsuoka, A. Errapart, C.R. Kurkjian, Micro-Photoelastic Evaluation of Indentation-Induced Stress in Glass, *Mater. Trans.* (2019) MD201903, 5 pp, <https://doi.org/10.2320/matertrans.MD201903>.
- [78] J. Ismail, F. Zaïri, M. Naït-Abdelaziz, Z. Azari, Computational modelling of static indentation-induced damage in glass, *Comp. Mater. Sci.* 42 (2008) 407-415, <https://doi.org/10.1016/j.commatsci.2007.08.006>.
- [79] A. Koike, M. Tomozawa, IR investigation of density changes of silica glass and soda-lime glass caused by microhardness indentation, *J. Non-Cryst. Solids* 353 (2007) 2318-2327, <https://doi.org/10.1016/j.jnoncrysol.2007.04.006>.
- [80] S. Yoshida, J.-C. Sanglebœuf, T. Rouxel, Quantitative evaluation of indentation-induced densification in glass, *J. Mater. Res.* 20 (2005) 3404-3412, <https://doi.org/10.1557/jmr.2005.0418>.
- [81] B. Mound, Cracking in Fused Quartz During Nanoindentation, PhD Thesis 2017, University of Tennessee, https://trace.tennessee.edu/utk_graddiss/4807. (accessed 31 January 2019)
- [82] K.W. Peter, Densification and Flow Phenomena of Glass in Indentation Experiments, *J. Non-Cryst. Solids.* 5 (1970) 103-115, [https://doi.org/10.1016/0022-3093\(70\)90188-2](https://doi.org/10.1016/0022-3093(70)90188-2).
- [83] M. Jebahi, D. André, F. Dau, J.-L. Charles, I. Iordanoff, Simulation of Vickers indentation of silica glass, *J. Non-Cryst. Solids* 378 (2013) 15-24, <https://doi.org/10.1016/j.jnoncrysol.2013.06.007>.

- [84] B. Marler, On the relationship between refractive index and density for SiO₂-polymorphs, *Phys. Chem. Miner.* 16 (1988) 286-290, <https://doi.org/10.1007/BF00220696>.
- [85] D. Tabor, *The Hardness of Metals* (Clarendon Press, Oxford, United Kingdom, 1951).
- [86] D. Kilymis, A. Faivre, T. Michel, S. Peugot, J.-M. Delaye, J. Delrieu, M. Ramonda, S. Ispas, Raman spectra of indented pristine and irradiated sodium borosilicate glasses, *J. Non-Cryst. Solids* 464 (2017) 5-13, <https://doi.org/10.1016/j.jnoncrysol.2017.03.012>.
- [87] L. Duponchel, P. Milanfar, C. Ruckebusch, J.-P. Huvenne, Super-resolution and Raman chemical imaging: From multiple low resolution images to a high resolution image, *Anal. Chim. Acta* 607 (2008) 168-175, <https://doi.org/10.1016/j.aca.2007.12.004>.
- [88] M. Offroy, M. Moreau, S. Sobanska, P. Milanfar, L. Duponchel, Pushing back the limits of Raman imaging by coupling super-resolution and chemometrics for aerosols characterization, *Sci. Rep.* 5 (2015) 12303, <https://doi.org/10.1038/srep12303>.
- [89] H. Cui, W. Zhao, Y. Wan, Y. Fan, L. Qiu, K. Zhu, Improving spatial resolution of confocal Raman microscopy by super-resolution image restoration, *Opt. Express* 24 (2016) 10767-10776, <https://doi.org/10.1364/OE.24.010767>.
- [90] S. Ben Khemis, E. Burov, H. Montigaud, D. Skrelic, E. Gouillart, L. Cormier, Structural analysis of sputtered amorphous silica thin films: A Raman spectroscopy investigation, *Thin Solid Films* 733 (2021) 13881, <https://doi.org/10.1016/j.tsf.2021.138811>.